Design and Implementation of a Tunable Vibration Absorber and a Time-Delayed Vibration Absorber

by
Jie Liu

A thesis
presented to Lakehead University
in partial fulfillment of the requirement for the degree of
Master of Science
in
Control Engineering

Thunder Bay, Ontario, Canada, 2005

Your file Votre référence
ISBN: 978-0-494-15629-2
Our file Notre référence
ISBN: 978-0-494-15629-2

Abstract

Excited by a harmonic disturbance, the primary structure will vibrate at the frequency of the driving force in the steady state. Traditionally, a passive absorber will be resorted to largely suppress this vibration in the event of the constant exciting frequency and the low damping in the system; however, when the driving frequency is shifting and/or there exists a high damping, it becomes impossible to bring the steady-state vibrations to rest or even to a desired small value only using a passive vibration absorber; instead, the semi-active or active vibration absorbers have been studied for decades, aiming to achieve better results in vibration suppression.

The first part of the thesis presents a newly-designed semi-active electromagnetic vibration absorber (EMVA), whose stiffness is on-line tunable. This facilitates the vibration suppression of the primary system excited by a harmonic force with a variable frequency. The EMVA consists of a clamped-clamped aluminum beam and a permanent magnet that is embedded in the center of the beam and placed between two poles of a C-shaped electromagnet. By varying the current of the electromagnet, stiffness of the EMVA can be adjusted instantaneously. A detailed procedure for the characterization of the EMVA is presented. The effective stiffness of the absorber is determined numerically and validated experimentally. To test the effectiveness in vibration suppression, the EMVA is used to track three types of the exciting frequency variations: one-step, multi-step and linear.

The second part of the thesis provides a new perspective on the design of a time-delayed active vibration absorber. This control system features one output feedback. The close relationship between the time-delayed active vibration absorber and the traditional PD controller is revisited with an assistance of a vector interpretation. The stability of the combined system is discussed. The attention is focused on the difficulty of maintaining the stability of the combined system while achieving a marginal stability of the absorber system. An electromagnetic active vibration absorber is developed. An online tuning strategy is implemented to automatically find the optimum gain while the delay time is fixed. The experimental results show that the proposed online tuning algorithm can ensure the stability of the combined system while maximizing vibration suppression.

Acknowledgements

I would like to thank my supervisor Professor Kefu Liu and co-supervisor Professor Hao Bai, for their enthusiastic supervisions and patient guidances. I could not have imagined having a better advisor and mentor for my graduate study, and without their common-sense, knowledge, perceptiveness and cracking-of-the-whip I would never have finished my thesis. Particularly, I would like to acknowledge the help of Professor Krishnamoorthy Natarajan, all the time, he is the right person I turn to for solving some problems in Electrical Engineering. I would like to thank Professor Abdelhamid Tayebi for providing the experimental instruments.

Thanks are also due to Technologists Mr. K. Bhatia and Mr. Jean Mark, for their kind help in building the experimental devices. In the meantime, I have to say many thanks to Mr. Gary Mezo, President of KILRED WINDING INDUSTRIES LTD, for providing us the materials for building the experimental apparatuses.

I am grateful to all my friends in the graduate program of Control Engineering, Lakehead University, for being the surrogate family during the two years I stayed here and for their continued moral support and technical discussion.

Finally, I am forever indebted to my wife, Lily Yin, for her understanding and endless encouragement, when it is most required.

Contents

List of Figures

List of Tables

Part I

A TUNABLE ELECTROMAGNETIC VIBRATION ABSORBER

Chapter 1

A Tunable Electromagnetic Vibration Absorber

1.1 Introduction

Excited by an external harmonic force, the machine and structures will vibrate at the same frequency in the steady state. In practice, this vibration can often lead to a number of undesirable circumstances. For example, vibration of an automobile or truck can cause driver discomfort and, eventually fatigue. Structural or mechanical failure can often result from sustained vibration (e.g. cracks in airplane wings). One approach to protecting a device from steady-state harmonic disturbance is a vibration absorber; further, considering the fact that the frequency of the sinusoidal force may change within a certain limit, it is desirable to design an absorber with its natural frequency tunable.

1.1.1 Literature Review

Tunable vibration absorbers belong to the family of semi-active control systems. Nowadays, semi-active control systems are attracting more and more research interests in the field of vibration control, since they combine the advantages of both passive and active control systems. On one hand, they keep the reliability of the passive systems even in the event of power loss; on the other hand, they maintain the versatility and adaptability of active systems without a great amount of power consumption. Generally, the mechanical properties of the semi-active systems, such as the stiffness and/or the damping value, can be adjusted based on the feedback from the measured response and/or the excitation. Several variable stiffness vibration absorbers have been

proposed. Stiffness variation of the device reported in [1] was achieved by varying the effective number of coils in a helical spring used as the absorber stiffness. The same vibration absorber was used to study non-collocated adaptive-passive vibration control in [2]. A vibration absorber developed in [3] consists of a flexible cantilever beam attached by a mass at its free end. By varying the length of the beam, the absorber frequency can be varied. A variable stiffness device proposed in [4] has four coil springs arranged in a planar rhombus configuration. The aspect ratio of the rhombus configuration can be varied by a linear electromechanical actuator to achieve a continuous variation of the absorber stiffness. In [5], a variable stiffness absorber similar to the one developed in [3] was used to compare two different tuning algorithms. It is noted that all the above tunable devices involve an electro-mechanical driven system. As a result, a slow reaction speed may become the main concern for this type of stiffness control devices. Alternatively, damping is sometimes added to the absorber systems to prevent resonance or to improve the effective bandwidth of operation [6]-[7]. Damping value can be made on-line adjustable by utilizing a variable-orifice valve to alter the resistance to the flow of a conventional hydraulic fluid damper [8]-[9]. Friction dampers have also been widely studied as another approach in semi-active vibration control [10]-[11]. Most noticeably, electro-rheological or magneto-rheological dampers feature a broad-bandwidth modulation of the damping characteristics through the variation of an electrical or magnetic field [12]-[14]. However, when adding the damping into the system, the performance of the absorber at the design frequency is sacrificed.

Over the past decades, various devices based on magnetism or electromagnetism have been used to suppress vibration. The electromagnetic servomechanism developed in [15] consists of two pairs of electromagnets and a lever. The current to each electromagnet is controlled separately. In this way, one pair of electromagnet and lever produces a pushing force while the other pair produces a pulling force vice versa such that an active dynamic vibration absorber is obtained. In [16], permanent magnets were used to build an extremely soft spring for the purpose of vibration isolation. A hybrid-type active vibration isolation system developed in [17] uses both electromagnetic and pneumatic forces. In [18], an electromagnetic device was designed to parametrically excite the experimental beam. The phenomenon of eddy current has been explored to develop magnetic dampers [19]-[21].

Similar to the devices reported in [1]-[5], the device developed in this study is a variable

stiffness one. However, a notable difference is that the present device is non-contact and non-mechanical motion and the change of the stiffness can be realized instantly. Also, different from the electromagnetic devices referred above, the present system is tunable on-line. In addition, a detailed procedure for the characterization of the stiffness is presented, which is lacking in [15]-[18]. The rest of this first part of the thesis is organized as follows: subsequently in this Chapter, the developed Electromagnetic Vibration Absorber (EMVA) is introduced and an experimental setup used to test the EMVA is explained; the procedure for the characterization of the EMVA is presented; In Chapter 2, an experimental calibration is conducted and the performance of the EMVA is tested; Finally, in Chapter 3, several design issues related to the tunable electromagnetic vibration absorber are discussed.

1.1.2 The Tunable Electromagnetic Vibration Absorber

Figure 1.1 shows a photograph of the developed electromagnetic vibration absorber attached to a primary system. The entire experimental system consists of three subsystems: EMVA, primary system, and computer control system. As schematically shown in Fig. 1.2, the EMVA comprises a clamped-clamped aluminum beam (1) and a permanent magnet (PM) (2) that is embedded in the center of the beam and placed between two poles of an electromagnet (3). The electromagnet is constructed by winding Gauge 18 copper wire around a C-shaped steel core. The permanent magnet plays a dual role: acting as an absorber mass and forming a variable magnetic spring by interacting with the electromagnet through varying the DC current of the electromagnetic coils. The primary system (4) is an aluminum slab supported by an aluminum plate on each side, acting like a single degree-of-freedom (DOF) system. The electromagnet is fastened to the slab by two brackets, forming part of the primary mass. A small permanent magnet (5) is glued on an aluminum bar that is clamped to the primary mass. This permanent magnet interacts with an electromagnetic shaker (6) to generate a non-contact exciting force. The purpose of adding the aluminum bar between the permanent magnet and the primary mass is to minimize the interference of the magnetic field generated by the electromagnetic shaker and the one generated by the absorber electromagnet. The parameters of the system are summarized in Table 1.1. The computer control system is explained as follows: the response of the absorber mass is measured by an accelerometer (B&K 4393V) which is located at the end of the face of PM, while another accelerometer located at the center of one bracket is used to feedback the response

of the primary system. The signals are conditioned via a charge amplifier (B&K Nexus2692). Subsequently, the Data Acquisition Board DS1102 (dSpace) is utilized to convert the signals from analog to digital or digital to analog. ControlDesk (dSpace) provides the interface between Matlab, Simulink and DS1102. A Simulink model was developed to implement on-line tuning. The sampled data are first stored in an S-function named "Buffer" until a specified data length such as N = 1024 or 2048 is reached, and the sampling rate in the experiment is 1 ms. Then the data are passed to an S function named "FFT" where FFT is conducted and the peak frequency in the FFT spectrum is determined. In the following step, the desired coil current is computed using the predetermined equation and sent to a current regulator board. The output of the board supplies the desired amplitude of the DC current to the electromagnetic coils. The exciting signal is generated by a subsystem within the Simulink model and sent to a power amplifier (B&K 2706). The output of the amplifier drives the electromagnetic shaker to excite the primary system.

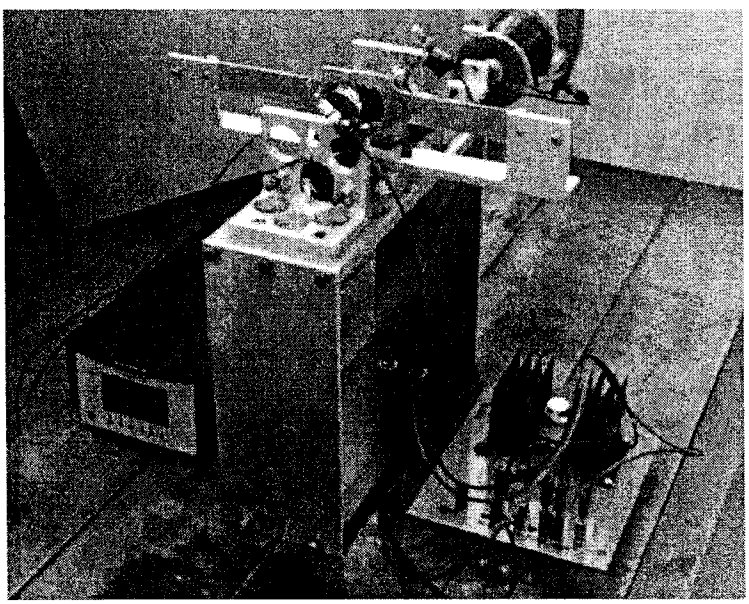

Figure 1.1: Photograph of the experimental setup.

1.2 Characterization of the EMVA

Characterization of the EMVA is very important for its design and implementation. As shown in Fig. 1.3, three springs are involved in the EMVA, namely, constant spring k_{c1} due to

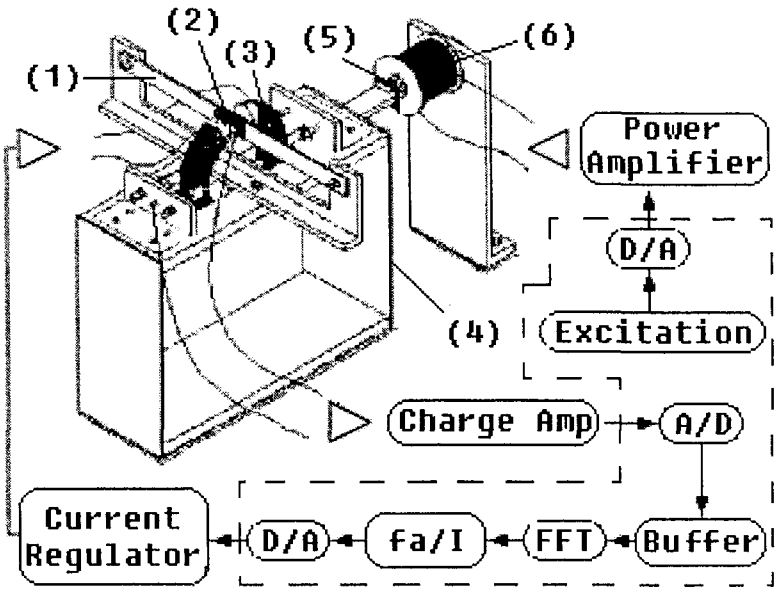

Figure 1.2: Schematic of the entire experimental system.

Symbol	Description	Quantity, Unit
m_a	Absorber mass	0.151 kg
m	Primary mass	3.074 kg
c_a	Damping coefficient of the absorber system	0.18 Ns/m
c	Damping coefficient of the primary system	3.71 Ns/m
R_1	Inner radius of the electromagnetic coils	11.0 mm
R_2	External radius of the electromagnetic coils	20.0 mm
L	Circumference of the electromagnet	314.16 mm
N	Turns of the coils	784
μ_0	Permeability of free space	$4\pi \times 10^{-7} H/m$
δ	The gap space between two pole faces of the electromagnet	42.0 mm
l	Length of PM	48.0 mm
w	Width of PM	22.0 mm
h	Thickness of PM	10.0 mm
R	Resistance of coils	4.62 Ω

Table 1.1: System parameters

the absorber beam, constant spring k_{c2} due to the interaction between the permanent magnet and the core of the electromagnet, and variable spring k_v due to the interaction between the permanent magnet and electromagnet. In what follows, attention is paid on determination of k_v and k_{c2}. The dynamics of the EMVA is explored to obtain the relationship between the magnetic force and the displacement of the absorber mass. With this relationship, the electromagnetic stiffness k_v is established.

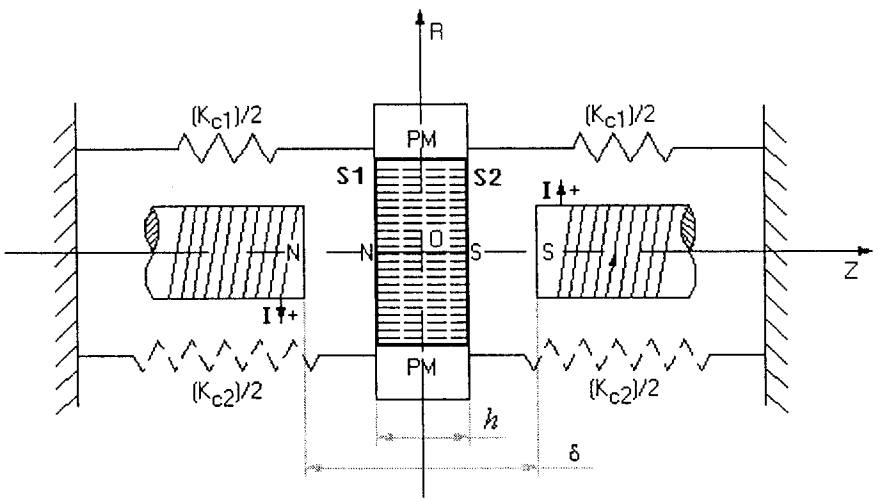

Figure 1.3: Three springs involved in the EMVA.

1.2.1 Magnetic Stiffness due to the Interaction between the Electromagnet and the PM

To determine the magnetic stiffness between the electromagnet and the PM, first the magnetic flux density of the electromagnet needs to be determined. The following analysis strategy is employed. The flux density from one pole of the electromagnet is determined by modeling the coils as a current carrying hollow cylinder with an inner radius R_1, an outer radius R_2, and a length L. The flux density of such a hollow cylinder can be found by examining first the magnetic field from a circular current loop with a radius a shown in Fig. 1.4. Expanding on the Biot-Savart law, which determines the magnetic field contribution of a current carrying element, the flux density B_{lr} (the subscript l means a loop) in the radial direction r and the flux density B_{lz} in the axial direction z can be expressed as [22]

$$B_{lr}(a,r,z) = \frac{\mu_0 i}{2\pi}\frac{z}{r}\frac{1}{[(a+r)^2+z^2]^{1/2}}\left[E_2\frac{a^2+r^2+z^2}{(a-r)^2+z^2} - E_1\right] \tag{1.1}$$

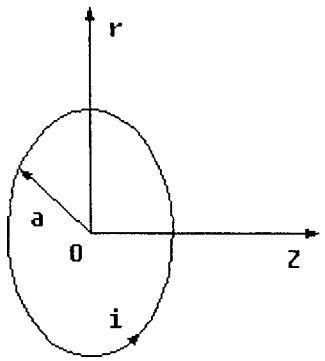

Figure 1.4: Circular current loop.

$$B_{lz}(a,r,z) = \frac{\mu_0 i}{2\pi} \frac{1}{[(a+r)^2+z^2]^{1/2}} \left[E_2 \frac{a^2-r^2-z^2}{(a-r)^2+z^2} + E_1 \right] \tag{1.2}$$

respectively, where E_1 and E_2 are the complete elliptic integrals of the first and second kind respectively, and they are of the forms:

$$E_1(a,r,z) = \int_0^{\pi/2} \left[1 - \frac{4ar}{(a+r)^2+z^2} \sin^2\theta \right]^{-1/2} d\theta \tag{1.3}$$

$$E_2(a,r,z) = \int_0^{\pi/2} \left[1 - \frac{4ar}{(a+r)^2+z^2} \sin^2\theta \right]^{1/2} d\theta \tag{1.4}$$

Now considering that the current carrying hollow cylinder is composed of infinite numbers of such circular current loops, the total contribution of the magnetic field of the cylinder can be found by integrating Eqs. (1.1) and (1.2) in both the radial and axial directions, as illustrated in Fig. 1.5,

$$B_{sr}(r,z) = \int_{R_1}^{R_2} \int_0^L B_{lr}(a,r,z+\lambda) d\lambda da \tag{1.5}$$

$$B_{sz}(r,z) = \int_{R_1}^{R_2} \int_0^L B_{lz}(a,r,z+\lambda) d\lambda da \tag{1.6}$$

where B_{sr} and B_{sz} (the subscript s means a single pole of the electromagnetic coils) are the radial and axial magnetic flux density from one pole of the current carrying coils, respectively, with the origin located at the center of the pole face. Note that in the equations above, the loop current should be substituted by

$$i = \frac{NI}{(R_2-R_1)L} \tag{1.7}$$

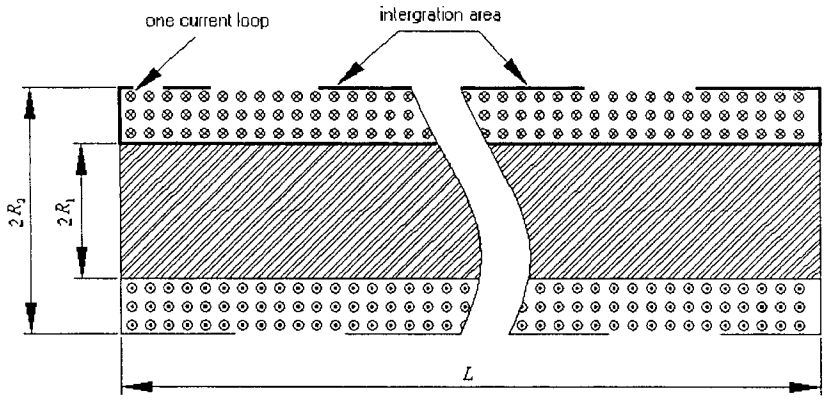

Figure 1.5: Instructive sketch of integration area.

where I is the coil current. The total magnetic flux densities B_{cr} and B_{cz} (the subscript c means the electromagnetic coils without the effect of the steel core) from the two poles of the current carrying coils can then be found by superposition. Taking the magnetic flux density along the centerline of air gap for example, Fig. 1.6 illustrates the axial magnetic flux density from the two poles of the electromagnet respectively; after adding these two components point to point, the total flux density B_{cz} can be obtained. Note that the negative signs for the flux density B_{cz} and the coil current I later on are with respect to the coordinates and the current direction defined in Fig. 1.3.

A ferromagnetic core can significantly magnify the magnetic field produced by the coils, and the amplification number μ_r, i.e., the relative permeability of the steel core, approaches to a constant at a certain region of operation. Further, for a certain coil current, the flux available in the air gap is solely affected by the term μ_r/γ and, the denominator γ is called leakage factor defined as the ratio of the total flux to the gap flux. Therefore, the total flux density functions in the radial and axial direction are given by

$$B_z = \frac{\mu_r}{\gamma} B_{cz}, B_r = \frac{\mu_r}{\gamma} B_{cr} \tag{1.8}$$

Since the value of μ_r/γ varies with materials of the core, specific experimental setup, etc., it is customary to determine it experimentally. Thus, a DC magnetometer (AlphaLab, Model: DCM) was used to measure the axial magnetic flux density at the points along the centerline of the gap, while, the ferromagnetic core is inserted in the center of the coils and four different amplitudes of DC currents are applied respectively. Fig.1.7 shows the measured axial flux densities and the

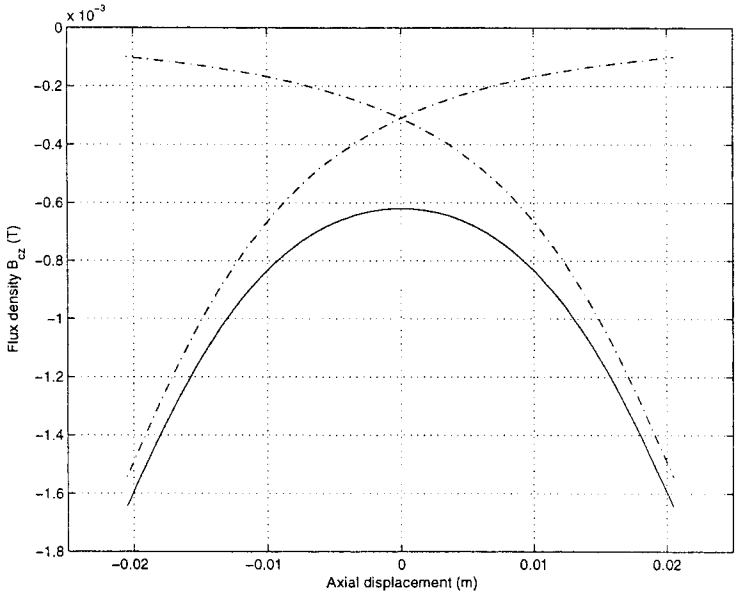

Figure 1.6: Axial magnetic flux density from the electromagnet, along the centerline of the gap: dashdot, flux density from one pole; dashed, that from the other pole; solid, the total axial flux density after superposition.

theoretical values calculated using Eq.(1.8), where the term μ_r/γ was found to be 27.3 in the following way: increase the value of μ_r/γ from zero step by step with the step size 0.1, each step the discrepancy between the experimental value and the analytical one was calculated; it was found that when $\mu_r/\gamma = 27.3$ the discrepancy is the smallest one, at 94% accuracy for the displacement range [-0.015, 0.015] m, where the origin is located at the center of the air gap, and the accuracy percentage is the ratio of $\sum_{i=1}^{17} |B_z^e(i) - B_z^a(i)|$ and $\sum_{i=1}^{17} |B_z^e(i)|$, where $B_z^e(i)$ is the ith experimental value and $B_z^a(i)$ is the corresponding axial flux density calculated by Eq. (1.8).

Considering the complexity of Eqs. (1.1-1.8), numerical methods are commonly employed to compute the distribution of the magnetic field around the gap area. The radial and axial components of the magnetic field induced by the electromagnet carrying -1.5 A of DC current are given in Figs. 1.8 and 1.9, respectively. From Fig. 1.8, it can be seen that the peaks of the radial flux density B_r occur on the pole faces at a distance of 15 mm, i.e., the mean radius of the coils and it diminishes to zero along the centerline of the coils. By contrast, the axial flux density B_z peaks along the centerline of the coils, reaches maximum on the pole faces and becomes minimum in the middle of the air gap.

With the flux density of the electromagnet available, the interaction force between the elec-

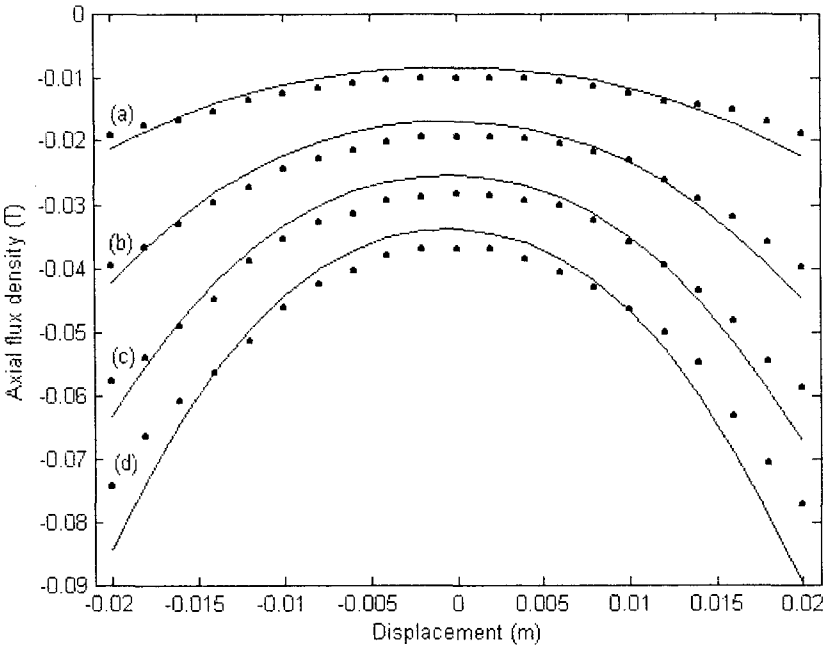

Figure 1.7: Magnetic flux density from the electromagnet, along the centerline of the gap, (a) I = -0.5 A, (b) I = -1.0 A, (c) I = -1.5 A, (d) I = -2.0 A: dot, experimental; solid line, analytical.

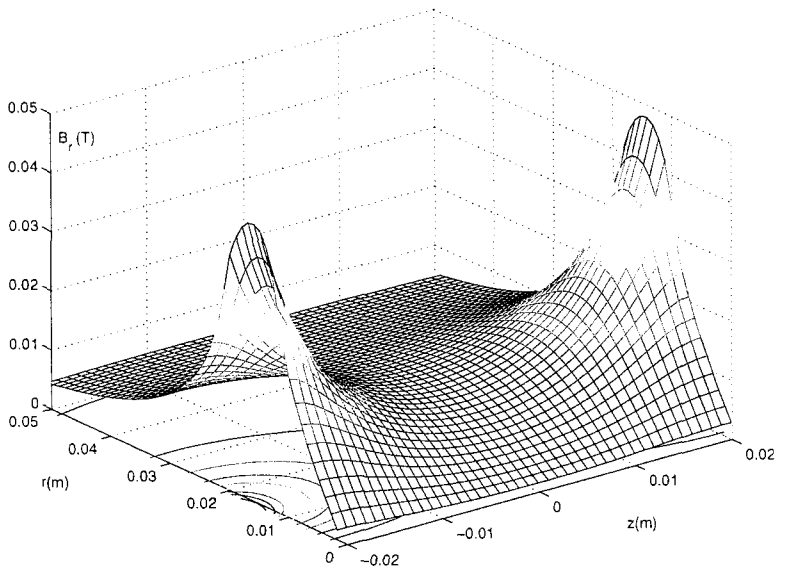

Figure 1.8: The radial magnetic flux density of the electromagnet, I = -1.5 A, the origin is at the gap center.

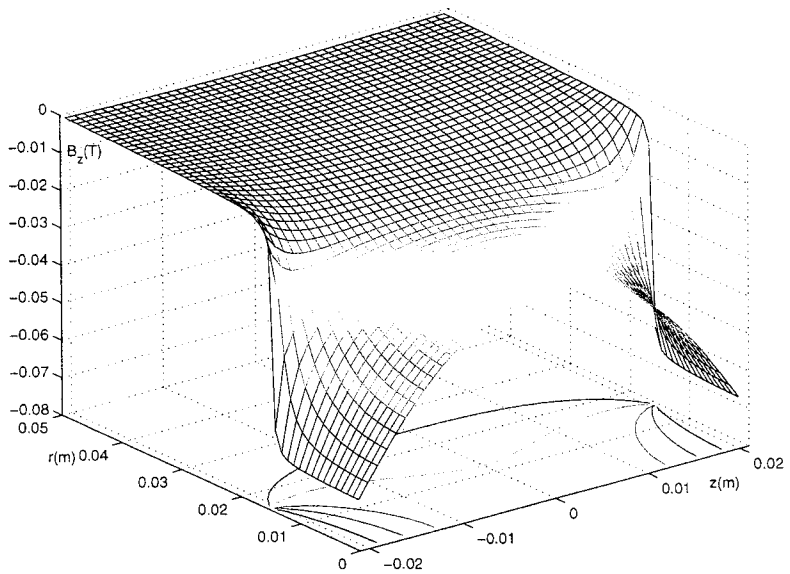

Figure 1.9: The axial magnetic flux density of the electromagnet, I = -1.5 A, the origin is at the gap center.

tromagnet and the PM is given by [22]

$$F_z = -\partial W/\partial z \tag{1.9}$$

where W is the energy of interaction of the electromagnet and the PM and may be calculated as the integral of the pole density on pole surfaces S_1 and S_2 (see Fig. 1.3) of the PM times the potential φ^{em} from the electromagnet, where φ^{em} is defined as

$$\varphi^{em} = \int H_z dz \tag{1.10}$$

where H_z is the magnetic strength with unit of Am^{-1}. If φ_1^{em} is the potential from the electromagnet at the pole face S_1 and φ_2^{em} that at the pole face S_2, then

$$W = \mu_0 \int_{S_1} M\varphi_1^{em} dS + \mu_0 \int_{S_2} (-M)\varphi_2^{em} dS \tag{1.11}$$

or

$$F_z = -\mu_0 \int_{S_1} M \frac{\partial \varphi_1^{em}}{\partial z} dS + \mu_0 \int_{S_2} M \frac{\partial \varphi_2^{em}}{\partial z} dS = M\left(\int_{S_1} B_{z1} dS - \int_{S_2} B_{z2} dS\right) \tag{1.12}$$

where $B_{zi} = -\mu_0 \frac{\partial \varphi_i^{em}}{\partial z}$, $i = 1, 2$, they are the electromagnetic flux density on the pole face S_1 and S_2 of the PM respectively. M is the magnetization of the PM (for the definition of magnetization,

see Appendix A). Equation (1.12) indicates that the force F_z is proportional to the difference between the total flux over the pole face S_1 and that over the pole face S_2. Note that, due to the symmetry of distributions of the radial magnetic flux, no net interaction force exists in the radial direction. Figure 1.10 shows the curves of the electromagnetic force F_z versus the displacement of the PM for four different amplitudes of the coil currents, calculated according to Eq. (1.12). As shown in the figure, within the range of [-0.01, 0.01] m, the force-displacement relationship is close to be linear. The linearized curves are shown in the Figure as well, and their slopes (see Table 2.1) are the electromagnetic stiffness k_v. It is also understandable that when positive currents are applied, similar curves with positive slopes are obtained and result in the positive electromagnetic stiffness k_v.

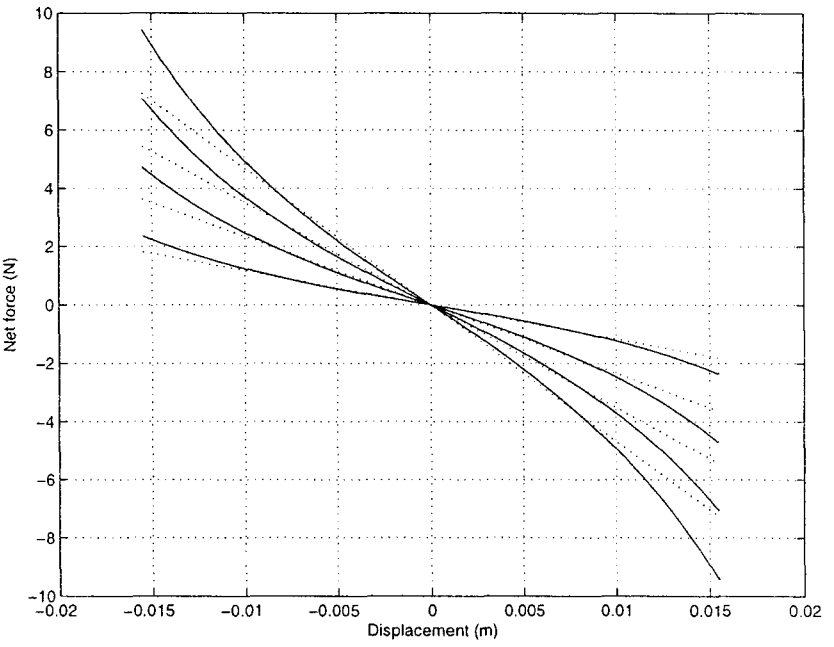

Figure 1.10: Interaction force F_z versus the displacement of the PM with the origin at the gap center: (a) I = -2.0 A, (b) I = -1.5 A, (c) I = -1.0 A, (d) I = -0.5 A: solid line, analytical; dotted line, linearized.

1.2.2 Magnetic Stiffness due to the Interaction between the PM and the Core

The orthorhombic PM $l \times w \times h$ (see Fig. 1.11)can be represented by two rectangles of surface pole density $\sigma = \pm M$ [22], where M is the magnet strength or magnetization of the PM with the unit Am^{-1}. The flux density on the central axis at a distance z from the PM can be

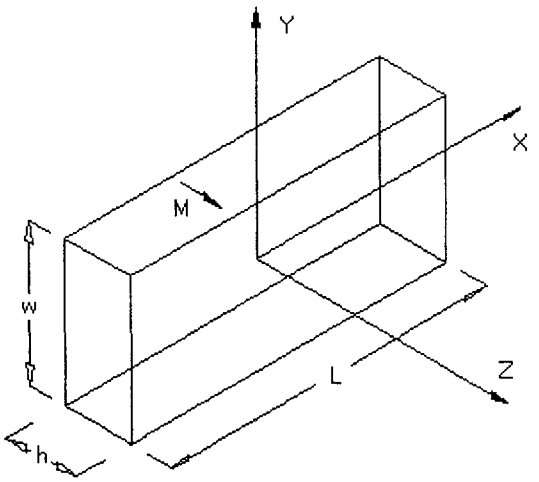

Figure 1.11: Orthorhombic permanent magnet

calculated as

$$B_{pm} = \frac{\mu_0 \sigma}{\pi} \left[\sin^{-1} \frac{lw}{\sqrt{(l^2 + 4z^2)(w^2 + 4z^2)}} - \sin^{-1} \frac{lw}{\sqrt{[l^2 + 4(z+h)^2][w^2 + 4(z+h)^2]}} \right] \quad (1.13)$$

As many factors affect the production of PMs, their final magnetic properties may vary. The Magnetic Materials Producers Association (MMPA) allows for up to 20% variation in magnetic energy from the published values for a grade of magnetic material, this large swing in magnetic properties can greatly affect the performance of any device using PMs. Because of this, the properties of a permanent magnet are normally determined experimentally. In order to identify the surface pole density σ, the magnetic flux density was measured by using the DC magnetometer at the points off the pole face and along the centerline of the PM. Comparing them with that obtained by Eq. (1.13), σ was found to be 395.8 kAm^{-1}, as shown in Fig. 1.12.

To understand the interaction force between the PM and the core, first, let consider the force between a PM and one end of a ferromagnetic cylinder, as shown in Fig. 1.13, this force may be approximated as [23]

$$F = \alpha B_S^2 A \quad (1.14)$$

where α is a constant to be determined, A the area of the PM surface, and B_S the flux density at the surface of the ferromagnetic cylinder. Let F_1 be the interaction force between the right end of the core and the PM and F_2 that for the left end, referred to Fig. 1.13. When the PM is

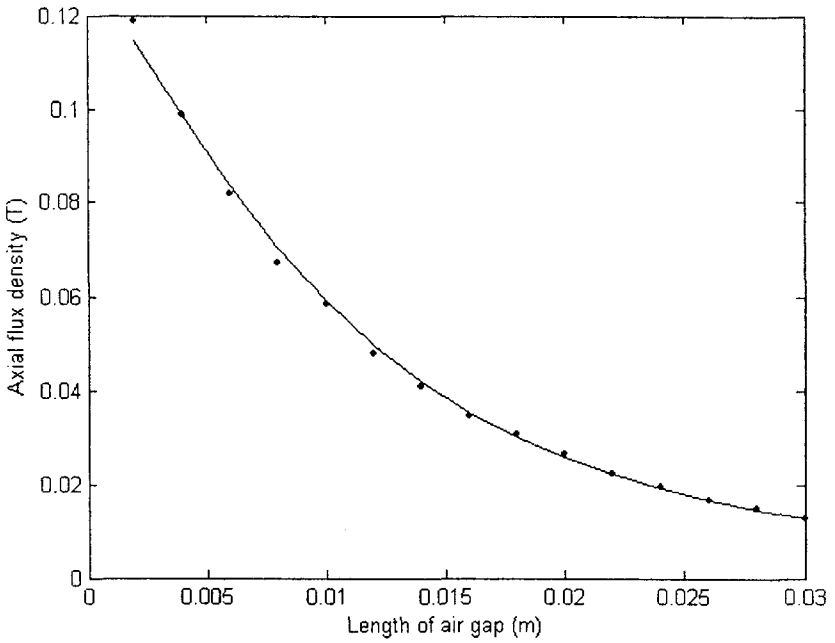

Figure 1.12: Magnetic flux density B_{pm} at the points along the centerline of the PM with the origin located at the center of the pole face: dot, experimental; solid line, analytical.

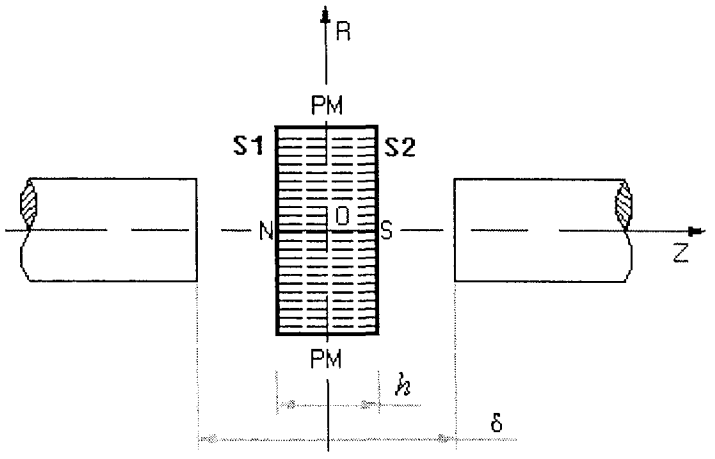

Figure 1.13: Interaction between the PM and the core

located in the exact middle of the air gap of the core, $F_1 = -F_2$ such that the net force is zero. When the PM is moved to right, $|F_1| > |F_2|$, vice versa. Using Eq. (5.1), the net force acting on the PM is given by

$$F = F_1 - F_2 = \alpha A(B_{S1}^2 - B_{S2}^2) \tag{1.15}$$

where B_{S1} and B_{S2} are the flux density at the right and left end of the core, respectively. Considering the fact that the magnetization in the ferromagnetic core induced by the magnetic field of the PM is not uniform and the core is curved, an experiment was set up to determine the relationship of the interaction force and the displacement. As shown in Fig. 1.14, the core was glued on a plastic plate and then placed on a precision electronic scale (OHAUS Model: GT4100). The PM was located in the pole gap with its position adjustable. First the scale reading without the PM was reset to be zero. Then the position of the PM was varied and the scale reading was recorded. When the air gap between the PM and the lower surface of the opening of the core was narrowed, the scale reading was reduced. This way, the interacting force between the PM and the core was found. The results are shown in Fig. 1.15. It can be seen that when the displacement of the PM center is within the range [-0.005, 0.005] m, the interaction force varies linearly with the change of the displacement, and has a tendency to pull the PM towards the core. Therefore this stiffness k_{c2} is approximated as a constant value of -417 N/m, as in Fig. 1.16. Equation (1.15) was used to curve-fit the data such that the constant α was found to be $\alpha = 0.913 \times 10^6\, mH^{-1}$.

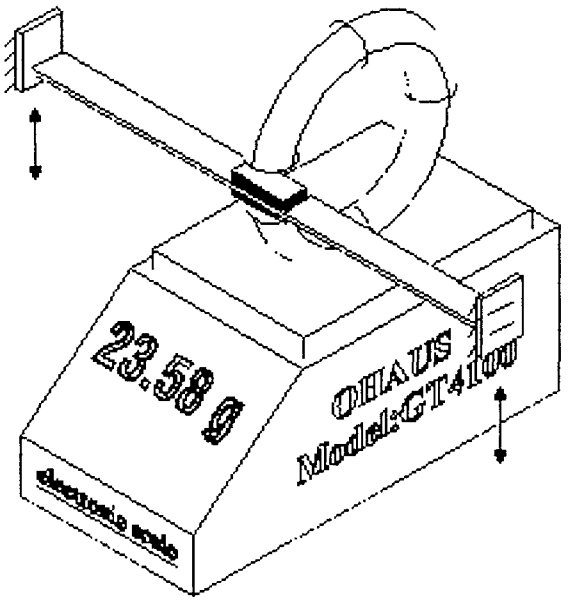

Figure 1.14: Experimental set up to measure the interaction force between the PM and the core.

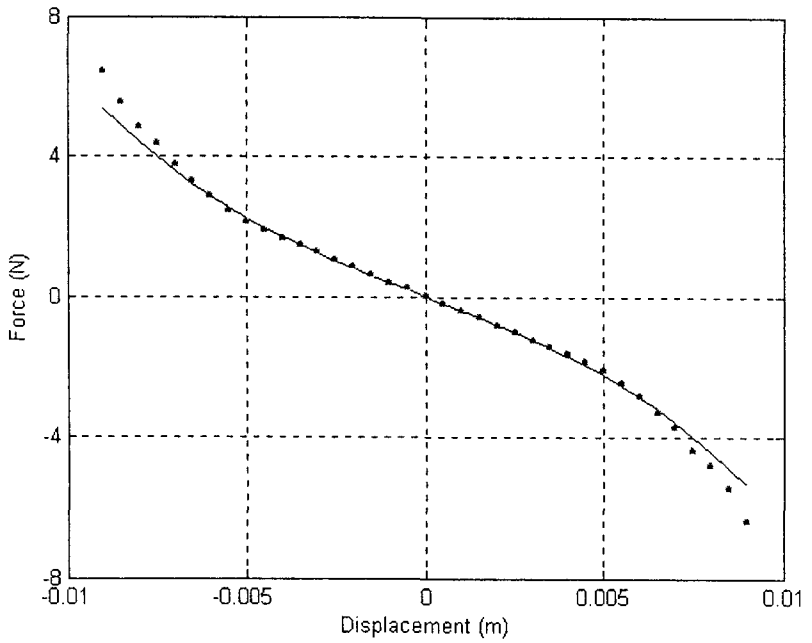

Figure 1.15: Interaction force of the PM and the core: dot, experimental; solid line, analytical.

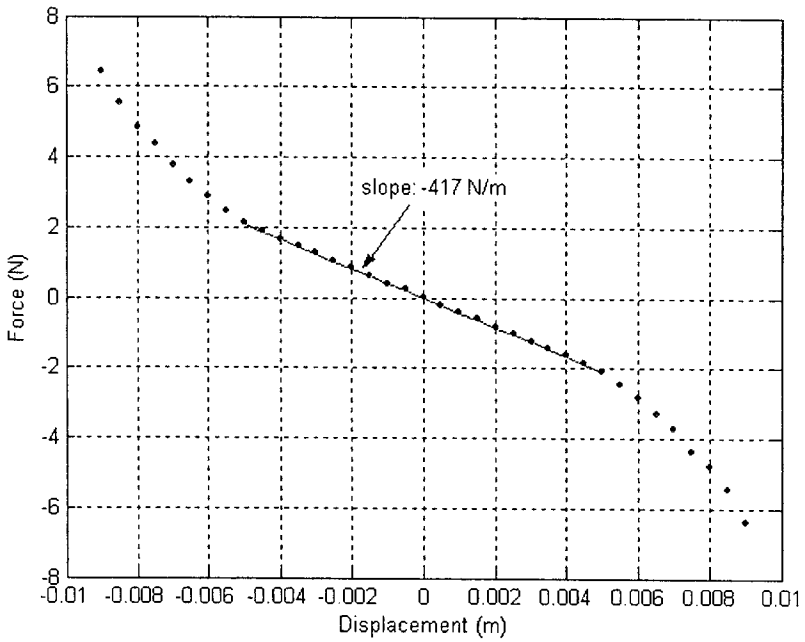

Figure 1.16: Interaction force of the PM and the core versus the displacement (Linearized)

Chapter 2

Experiment

An experiment was carried out to serve for three purposes: initial testing of the absorber system and the entire system, experimental determination of the relationship between coil current and the absorber natural frequency, and evaluation of the effectiveness of the EMVA in the vibration suppression.

2.1 Preliminary Testing

An impulse excitation is a force that is applied for a very short length of time and represents one example of a shock loading. The response of a system to an impulse is identical to the free response of the system to certain initial conditions. In vibration testing, a mechanical device under test is often given an impact, and the response is measured to determine the system's vibration properties. When the absorber system is not attached, hit the primary system with a hammer, and the hitting point is selected at the very end of one supporting plate where the primary mass is fixed. The impact response of the primary system is measured using the accelerometer and plotted in Fig. 2.1; Through Fast Fourier Transform (FFT), the natural frequency of the primary system was found to be f_p=16.0 Hz, which can be seen from Fig. 2.2. In order to prevent its resonance, the absorber frequency must be tuned to be f_a=16.0 Hz when no current is applied to the electromagnet coils. To achieve it, k_{c1} was adjusted by manually tensioning the absorber beam such that f_a=18.1 Hz in the case that the electromagnet is not in place, the impact response and the corresponding FFT spectrums are shown in Fig. 2.3 and Fig. 2.4, respectively. After the electromagnet is installed and the negative stiffness k_{c2} takes effect, the absorber frequency was reduced to 16.0 Hz, as illustrated in Fig. 2.5 and Fig. 2.6.

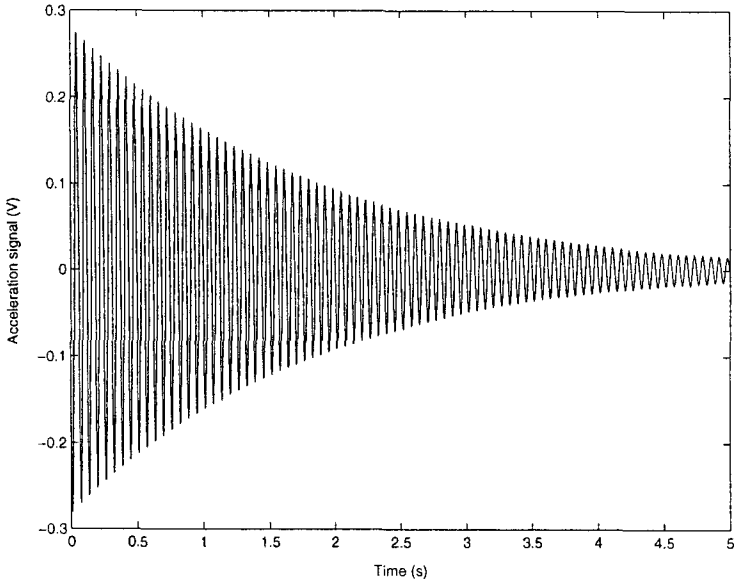

Figure 2.1: Impact response of the primary system, without the absorber system attached.

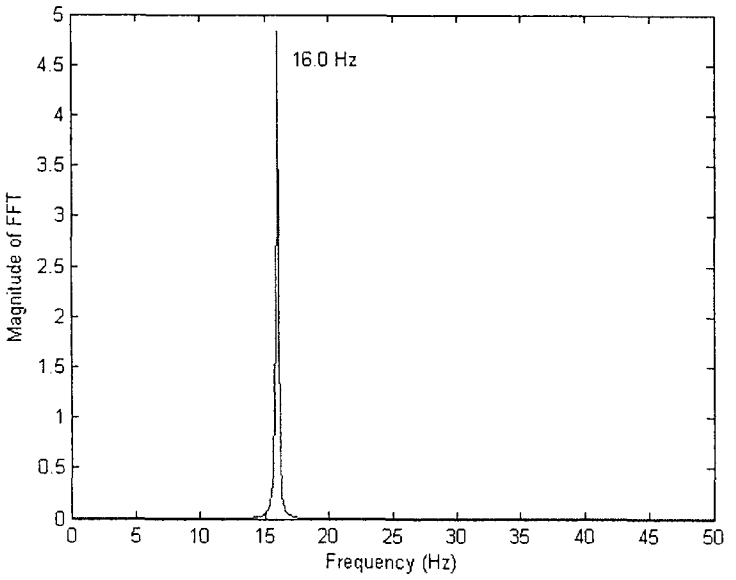

Figure 2.2: Spectrum of an impact response of the primary system in FFT.

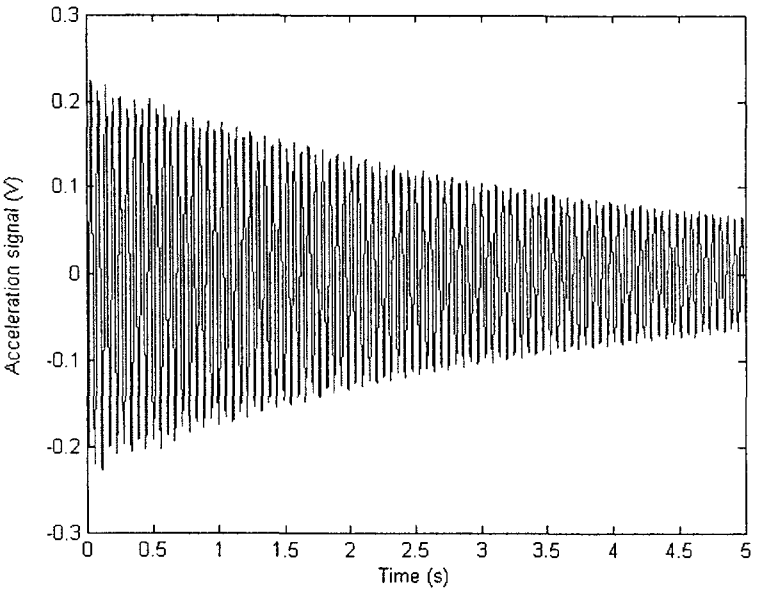

Figure 2.3: Impact response of the absorber beam, without the electromagnet in place.

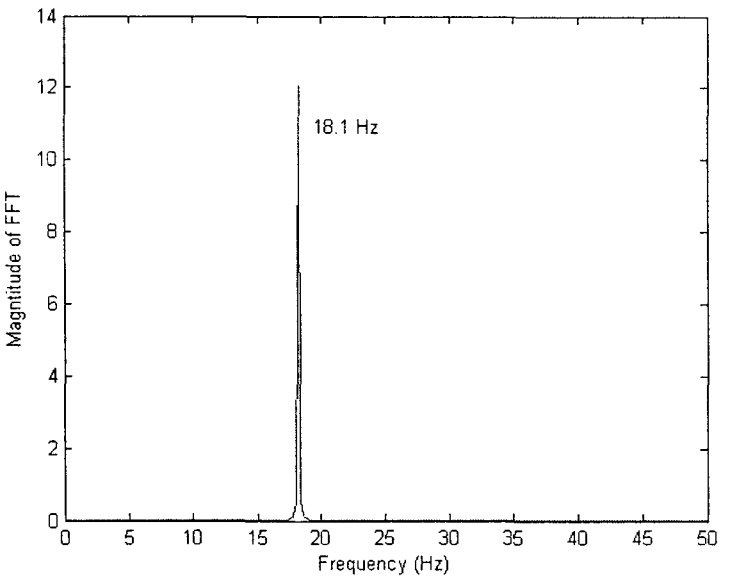

Figure 2.4: Spectrum of an impact response of the absorber beam in FFT, without the electromagnet in place.

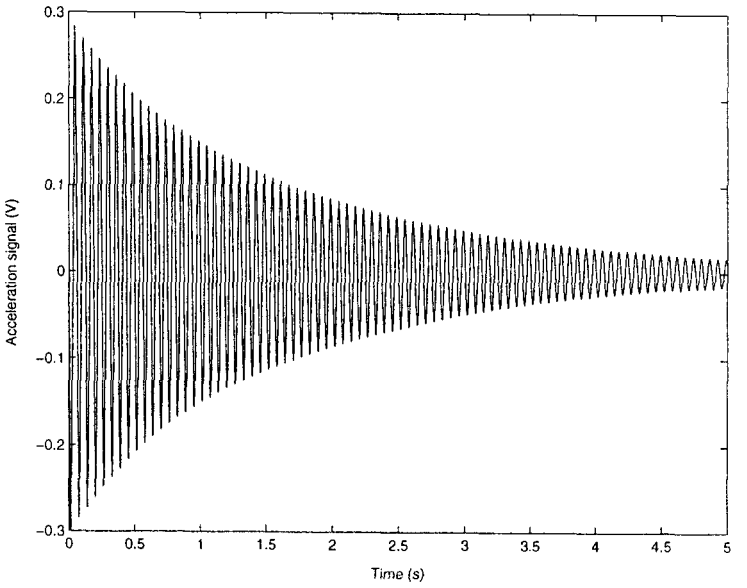

Figure 2.5: Impact response of the absorber system.

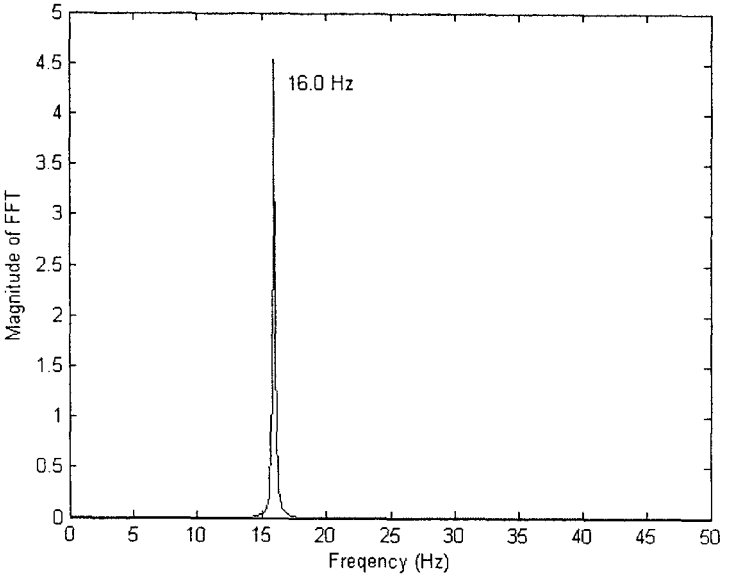

Figure 2.6: Spectrum of an impact response of the absorber system in FFT.

To determine experimentally the magnetic stiffness k_v, the natural frequencies of the absorber system corresponding to different coil currents were found by impact testing as well. The primary mass was fastened firmly on the ground through a rigid support. The current to the electromagnet was increased from 0 A to 2.3 A at a step of 0.1 A, then decreased to -2.3 A at the same step size. Finally the current was loaded up from -2.3 A to 2.3 A at the same pace. For each given current, the absorber mass was tapped and the acceleration signals of the absorber mass were recorded. By applying the FFT to the measured response, the natural frequency f_a of the absorber was found. Figure 2.7 shows the curves of the absorber frequency f_a versus the loading and unloading of the coil current. It exhibits the characteristic of slight hysteresis due to the nature of the steel core. A comparison of the variable stiffness k_v obtained analytically and experimentally is demonstrated in Table 2.1; it indicates that the analytical characterization agrees well with the experimental calibration.

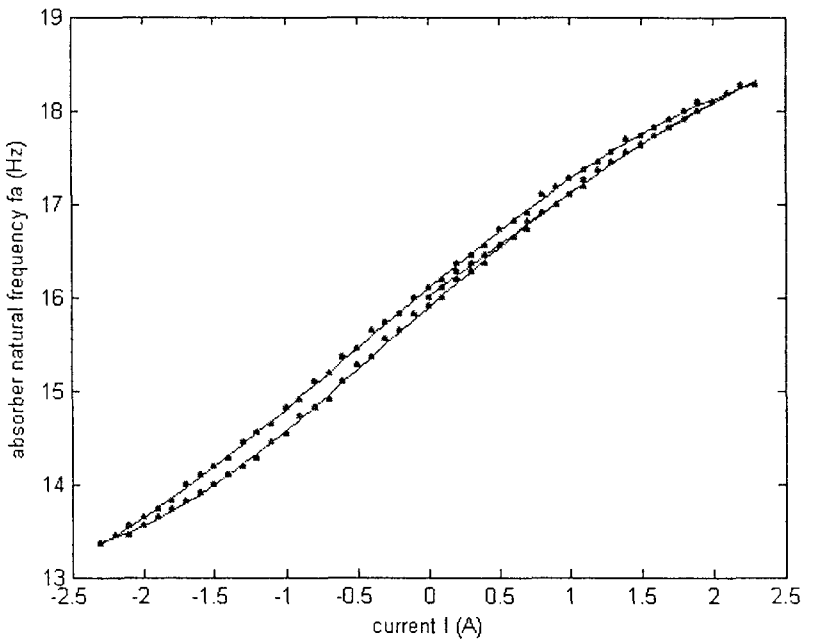

Figure 2.7: Absorber frequency versus the coil current during the loading and unloading periods.

The componential stiffnesses in the experimental system are summarized in Table 2.2. The stiffness k of the primary system, the stiffness k_{c1} of the absorber beam and the invariable stiffness

Coil Current (A) (A)	Theoretical Data (N/m) (N/m)	Experimental loading	Data (N/m) unloading
- 0.5	- 117.04	-136.08	-103.11
- 1.0	- 234.08	-265.80	-216.80
- 1.5	- 351.10	-357.67	-327.44
- 2.0	- 468.15	-431.58	-416.99
0.5	117.04	106.72	142.43
1.0	234.08	215.01	251.88
1.5	351.10	328.88	347.86
2.0	468.15	424.73	424.73

Table 2.1: Variable stiffness k_v

Symbol	Description	Quantity, Unit
k_{c1}	stiffness of absorber beam	1953 N/m
k_{c2}	invariable stiffness caused by interaction of PM and steel core	-426 N/m
k_c	constant part of absorber stiffness	$k_{c1} + k_{c2}$ N/m
k_v	variable part of absorber stiffness controlled by coil current	$[-430, 430]$ N/m
k_a	total stiffness of absorber system	$k_c + k_v$ N/m
k	stiffness of primary system	31067.0 N/m

Table 2.2: The componential stiffnesses in the experimental system

k_{c2} caused by the interaction of PM and the steel core are caculated using Eq. (2.1),

$$k' = m'\omega'^2 \tag{2.1}$$

where k', m' and ω' are the corresponding stiffness, mass and the natural frequency of the object.

In order to help understand the extent to which the analytical characterization of the EMVA can predict its dynamics, the variable stiffness k_v, obtained in the experimental and analytical ways, is plotted in Fig. 2.8 respectively, it shows that the experimental results closely coincide with those obtained analytically provided that the coil current is within [-1.5, 1.5] A; however, when the needed current is beyond that range, the values achieved by two different methods will start to differ, because the ferromagnetic core becomes saturated.

The constitutive components of the stiffness of the entire EMVA are illustrated in Fig. 2.9,

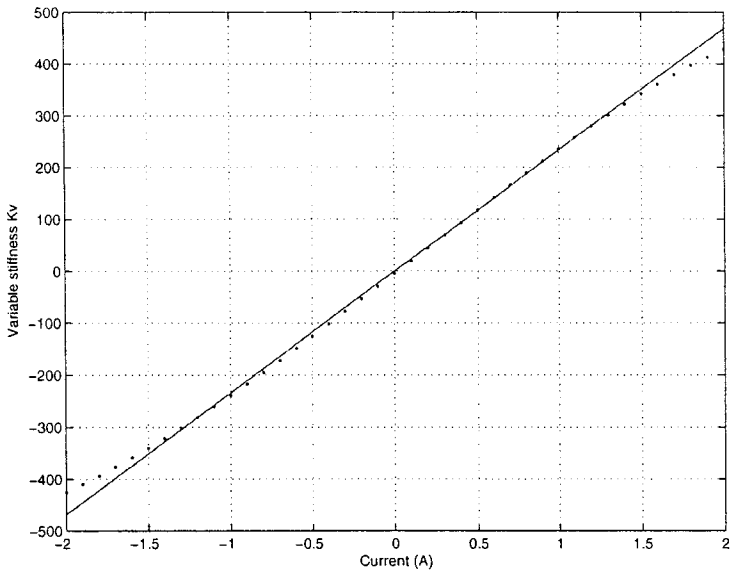

Figure 2.8: The variable stiffness k_v obtained experimentally and analytically: dot, experimental; solid line, analytical

and it also shows the adjustable margin for k_v and the resulting adjustable range for k_a.

Since k_a can be varied when different DC currents go through the coils, the natural frequencies of the whole system will correspondingly experience a variation. An experiment was carried out next to find out those natural frequencies. Set the coil current to be -2A, 0A and 2A, respectively; keeping each current constant, the combined system was driven by the external force with a frequency changing from a low frequency (12Hz,13Hz and 14Hz) to a high frequency (18Hz,19.2Hz and 21Hz) at a step of 0.1 Hz; for each step, the steady-state amplitude of the acceleration signal was measured and recorded. The curves for the magnitudes of the acceleration signals versus the driving frequencies were plotted in Fig. 2.10. It shows that without a current in the coils the resonance frequencies of the entire system are 14.5 Hz and 17.9 Hz, respectively; moreover, the magnitude reaches its lowest point at 16.0 Hz, which is the anti-resonance frequency. Undoubtedly, the natural frequencies of the entire system can be found by an impact testing as well. The impact response of the whole system without coil current was recorded and then shown in Fig. 2.11. Applying FFT on the response, as in Fig. 2.12, it can be found that the frequencies corresponding to the peak spectrums are 14.5 Hz and 17.9 Hz, this coincide with the analysis above. It should also be noted, when the coil current $I = -2$ A, the resonance

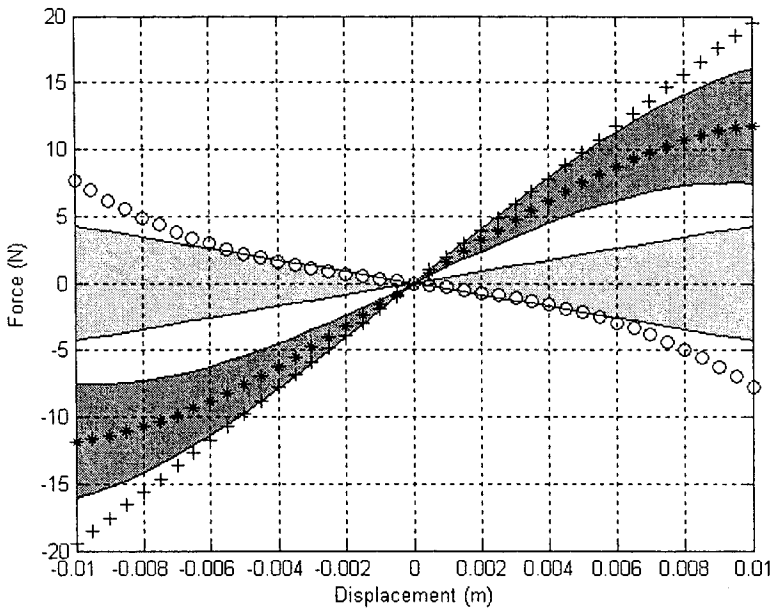

Figure 2.9: Constitutive components of the spring force of the EMVA: plus, force associated with k_{c1}; circle, force associated with k_{c2}; star, force associated with k_c; gray area, adjustable margin for k_v; dark area, adjustable margin for k_a.

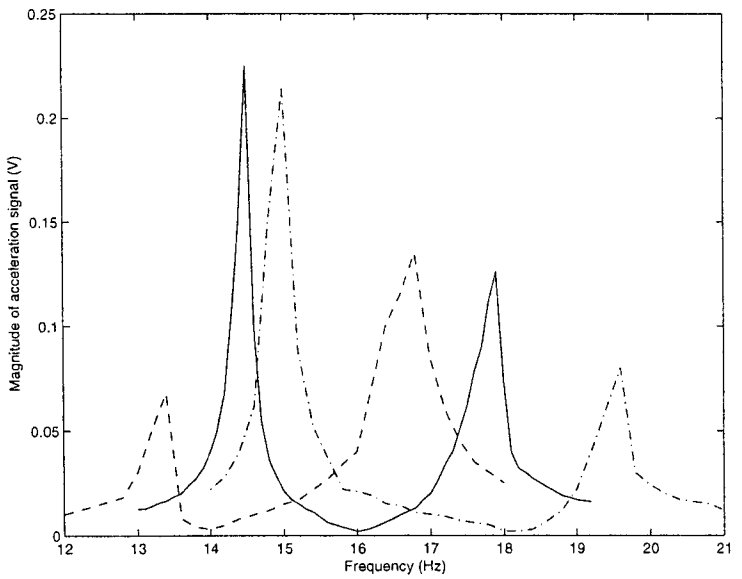

Figure 2.10: Magnitude of the acceleration signals versus the driving frequencies: dashed line, I=-2A; solid line, I=0A; dashdot line, I=2A.

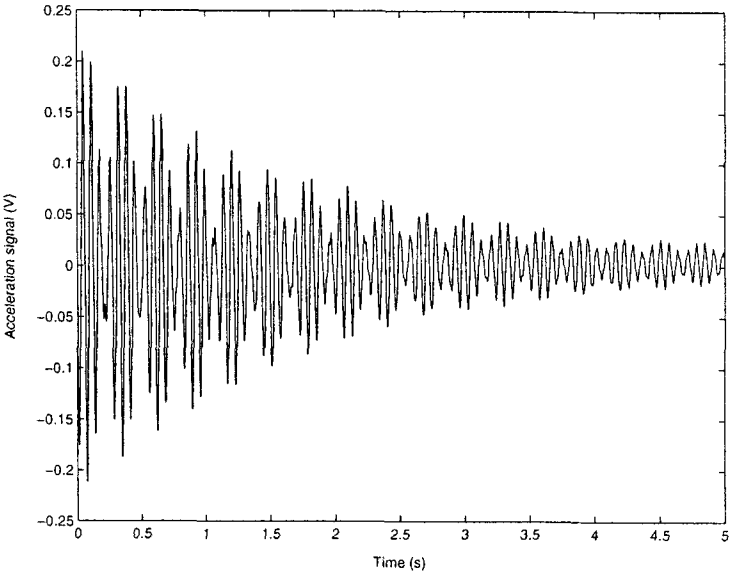

Figure 2.11: Impact response of the whole system.

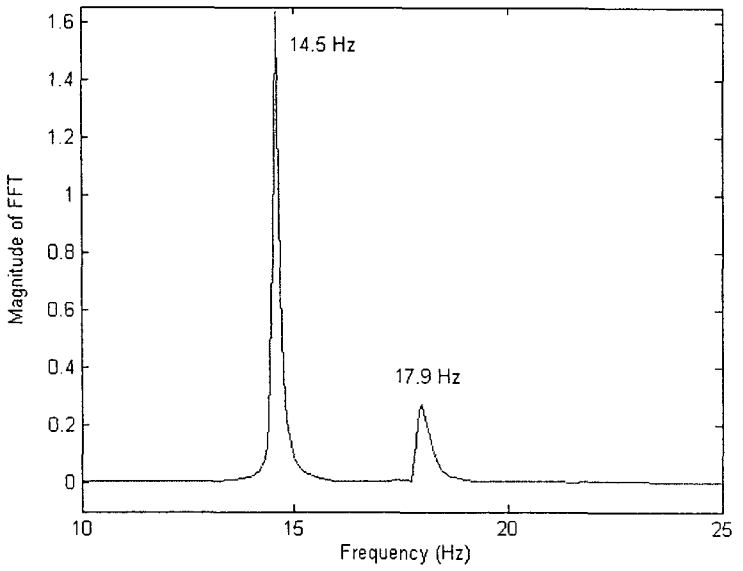

Figure 2.12: spectrums of an impact response of the whole system in FFT.

frequencies shift to the left, at 13.4 Hz and 16.8 Hz, respectively; when the coil current $I = 2$ A, the resonance frequencies shift to the right, at 15 Hz and 19.6 Hz, respectively; further, in each case, the highest peak frequency is the one close to 16.0 Hz.

2.2 Application of the EMVA

The control strategy originates from the traditional design of the passive vibration absorbers. In the case that the system damping is low, the passive vibration absorber can eliminate the vibrations of the primary structure at the design frequency, however, once the exciting frequency shifts away, the primary system may experience severe oscillations. Instead, the tunable EMVA can correspondingly change its frequency to follow the variation of the exciting frequency; as a result, the vibrations of the primary system are effectively suppressed.

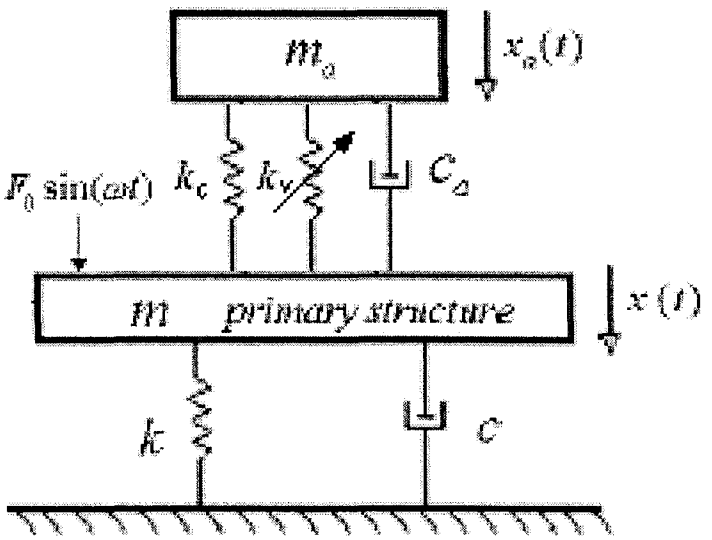

Figure 2.13: 2-DOF system with variable stiffness k_v.

As shown in Fig. 2.13, the governing equations of the dynamics of the 2-DOF system with variable stiffness k_v is given by

$$\begin{bmatrix} m & 0 \\ 0 & m_a \end{bmatrix} \begin{bmatrix} \ddot{x}(t) \\ \ddot{x}_a(t) \end{bmatrix} + \begin{bmatrix} c + c_a & -c_a \\ -c_a & c_a \end{bmatrix} \begin{bmatrix} \dot{x}(t) \\ \dot{x}_a(t) \end{bmatrix} + \begin{bmatrix} k + k_a & -k_a \\ -k_a & k_a \end{bmatrix} \begin{bmatrix} x(t) \\ x_a(t) \end{bmatrix} = \begin{bmatrix} F_0 \sin(\omega t) \\ 0 \end{bmatrix} \tag{2.2}$$

where $F_0 \sin(\omega t)$ is the external sinusoidal force and $k_a = k_c + k_v$. Mathematical manipulation

leads to the steady state displacement of the primary structure in the frequency domain,

$$X = \frac{k_a - m_a\omega^2 + jc_a\omega}{\begin{vmatrix} k + k_a - m\omega^2 + j(c + c_a)\omega & -k_a - jc_a\omega \\ -k_a - jc_a\omega & k_a - m_a\omega^2 + jc_a\omega \end{vmatrix}} F_0 \tag{2.3}$$

where $j = \sqrt{-1}$. The EMVA may introduce a small damping c_a into the system, which causes the complete elimination of the steady state vibration of the primary structure impossible; however, the main concern should be given on the term $k_a - m_a\omega^2$ in the numerator of Equation (2.3). Thus the tuning condition is given as

$$\omega_a = \sqrt{\frac{k_c + k_v}{m_a}} = \omega \tag{2.4}$$

The objective of the auto-tuning strategy is to ensure that the natural frequency of the absorber equals the exciting frequency, i.e., $f_a = f$, through adjusting the electromagnet current. The excitation frequency can be detected by performing FFT on the recorded response of the absorber mass, and the frequency corresponding to the maximum peak of the spectrum of the response is regarded as f. The relationship between the current and the absorber frequency was obtained by conducting a third-order polynomial least-square curve fitting on the averaged points of the loading and unloading curves. Figure 2.14 shows the average points and the best fit curve. The best fit curve equation is given as

$$I = -117.3428 + 21.0199f_a - 1.2995445f_a^2 + 0.0277619f_a^3 \tag{2.5}$$

Further, when the interaction force between the electromagnet and the PM is known, the absorber frequencies corresponding to various current can be calculated analytically, it is depicted in Fig. 2.15, and the mathematical equation is represented by

$$I = -6.52355 + 0.02546722f_a^2 \tag{2.6}$$

As shown in Fig. 1.2, the response of the absorber mass is measured by an accelerometer (B&K 4393V), and conditioned via a charge amplifier (B&K Nexus2692). Subsequently, the Data Acquisition Board DS1102 (dSpace) is utilized to convert the signals from analog to digital or digital to analog. ControlDesk (dSpace) provides the interface between Matlab, Simulink and DS1102. A Simulink model was developed to implement on-line tuning. The sampled data are

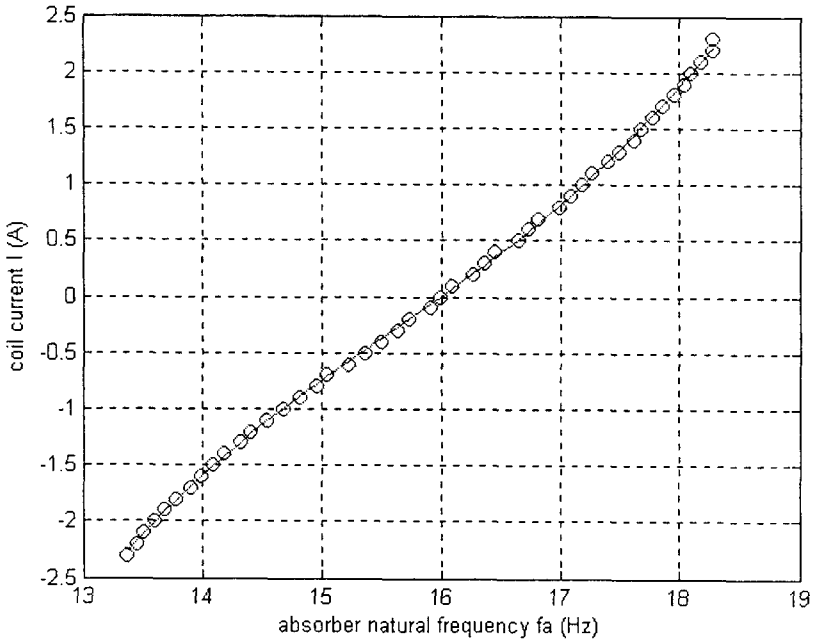

Figure 2.14: Relationship between the coil current and the absorber natural frequency: circle, experimental, line, the best-fit curve.

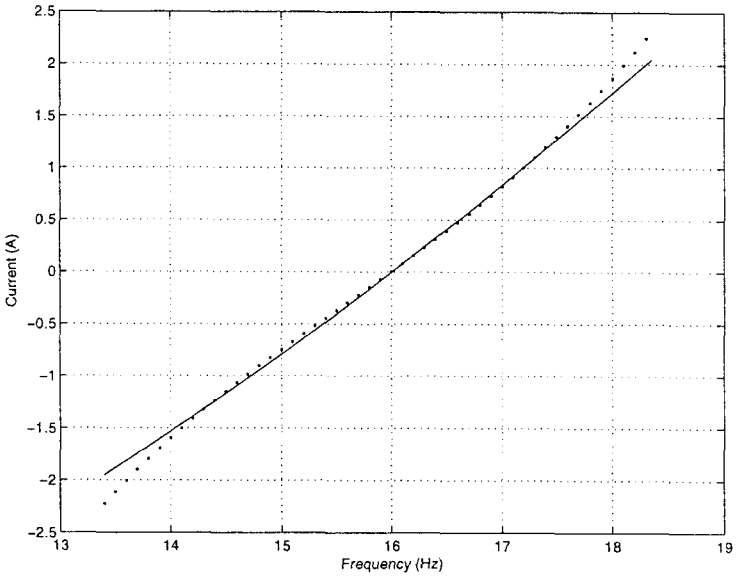

Figure 2.15: The absorber frequencies obtained experimentally and analytically: dot, experimental; solid line, analytical

first stored in an S-function named "Buffer" until a specified data length such as $N = 1024$ or 2048 is reached, and the sampling rate in the experiment is 1 ms. Then the data are passed to an S-function named "FFT" where FFT is conducted and the peak frequency in the FFT spectrum is determined. In the following step, the desired coil current is computed by Eq. (2.5) or (2.6) and sent to a current regulator board. The output of the board supplies the desired amplitude of the DC current to the electromagnetic coils. The exciting signal is generated by a subsystem within the Simulink model and sent to a power amplifier (B&K 2706). The output of the amplifier drives the electromagnetic shaker to excite the primary system.

Based on Eq.(2.5), three testing scenarios were devised to demonstrate the effectiveness of the EMVA in suppressing the vibrations caused by a shifted excitation frequency: one-step change, multiple-step change and linear change. In the one-step change the exciting frequency is changed from 16.0 Hz to 14.5 Hz, this is to simulate the situation: in the beginning, the absorber system is working at its originally designed frequency, now no current goes through the coils and, the absorber acts solely as a passive one; at the instant of 5 s, the exciting frequency experiences a sudden variation from the anti-resonance frequency to the first natural frequency. With the stiffness of the absorber system unchanged, the primary system will be at resonance and vibrate severely; however, when the EMVA is activated, the vibrations of the primary mass are suppressed in a very short time, as can be seen in Fig. 2.16. The multi-step change is composed of three step changes of the exciting frequency. For the period of $t < 5$ s, the exciting frequency was 13.5 Hz. At $t = 5$ s, the exciting frequency was suddenly changed to be 14.5 Hz. At $t = 20$ s, it was changed to be 16.0 Hz. At $t = 35$ s, it was changed to be 17.9 Hz. Figure 2.17 shows the experimental results. When the EMVA was not controlled, the absorber frequency was 16.0 Hz. The first step change brought the system into resonance and the response was increased significantly. The second step change resulted in the anti-resonance and the response was decreased. The third step change once again forced the system into resonance and the response saw another surge. When the auto-tuning control was activated, the EMVA is capable of adjusting its stiffness such that vibration of the primary mass was promptly suppressed at each stage. As the data length used was $N = 2048$, the reaction time for tuning was 2.048 s. It should be noted that the reaction time is solely dependent of the tuning algorithm while for those motor-driven devices [1]-[5], an extra time is needed for the desired stiffness to be reached. For the linear

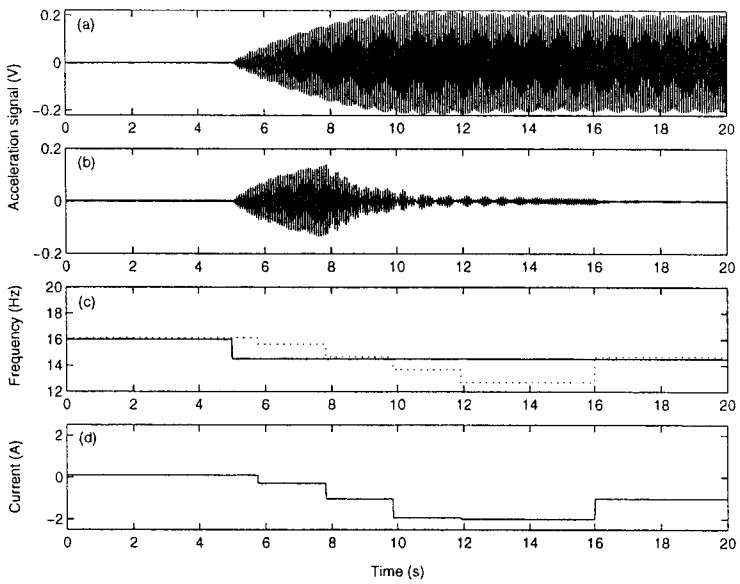

Figure 2.16: Experimental results for the one step change of the exciting frequency, N=2048 and using Eq. (2.5): (a) response of the primary mass without control of EMVA; (b) response of the primary mass with control of EMVA; (c) the exciting frequency (solid) and the measured frequency (dotted); (d) coil current.

change, the exciting frequency was varied linearly from 13.5 Hz to 17.9 Hz. Figure 2.18 shows the results. It is noted that the tuning algorithm based on FFT failed to follow the variation of the exciting frequency. When the exciting frequency was continuously changed, the transient responses were excited out such that the response was dominated by a component associated with one of the natural frequencies. The peak frequency in the FFT spectrum corresponded to the natural frequency instead of the exciting frequency. Such a limitation of the FFT based algorithm was addressed in [5].

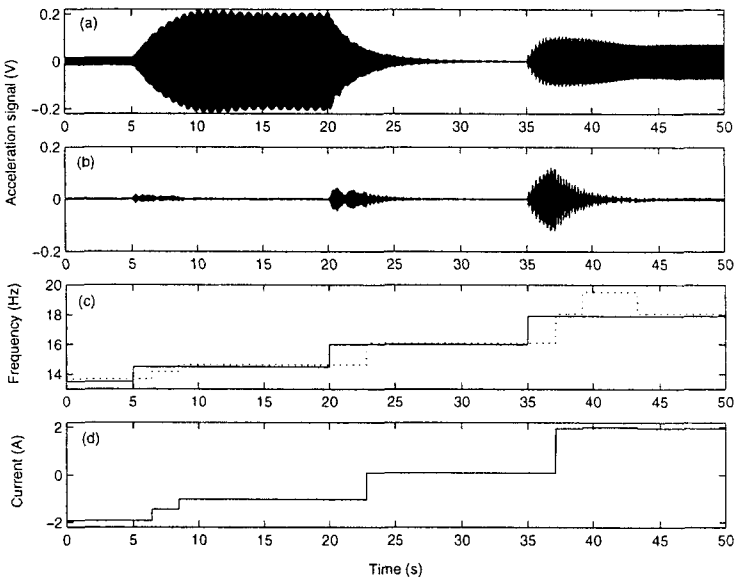

Figure 2.17: Experimental results for the multi-step change of the exciting frequency, N=2048 and using Eq. (2.5): (a) response of the primary mass without control of EMVA; (b) response of the primary mass with control of EMVA; (c) the exciting frequency (solid) and the measured frequency (dotted); (d) coil current.

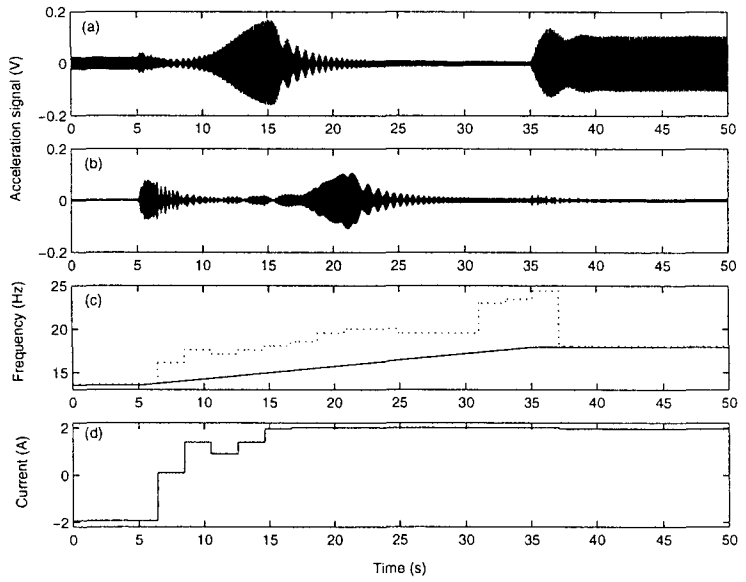

Figure 2.18: Experimental results for the linear change of the exciting frequency, N=2048 and using Eq. (2.5): (a) response of the primary mass without control of EMVA; (b) response of the primary mass with control of EMVA; (c) the exciting frequency (solid) and the measured frequency (dotted); (d) coil current.

The same experimental scenarios were again conducted based on the Equation (2.6), to compare the two different ways obtaining the relationships between the coil current and absorber frequency. The results are shown in Fig. 2.19 - Fig. 2.21, they prove that the effectivenesses in term of vibration suppression are almost the same between the experimental method and analytical method.

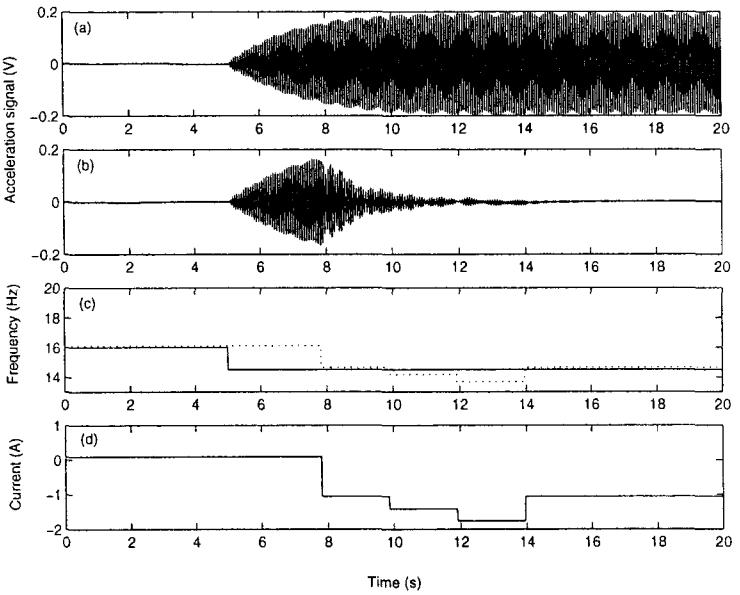

Figure 2.19: Experimental results for one step change of the exciting frequency, N=2048 and using Eq. (2.6): (a) response of the primary mass without control of EMVA; (b) response of the primary mass with control of EMVA; (c) the exciting frequency (solid) and the measured frequency (dotted); (d) coil current.

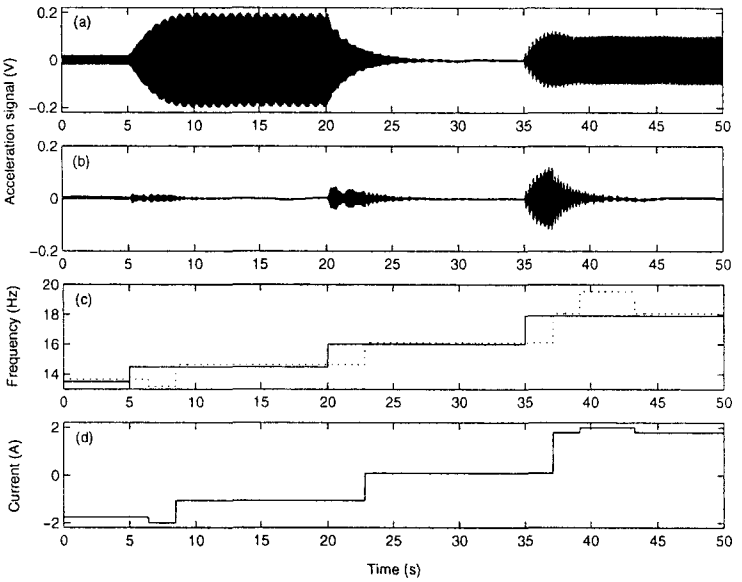

Figure 2.20: Experimental results for multi-step change of the exciting frequency, N=2048 and using Eq. (2.6): (a) response of the primary mass without control of EMVA; (b) response of the primary mass with control of EMVA; (c) the exciting frequency (solid) and the measured frequency (dotted); (d) coil current.

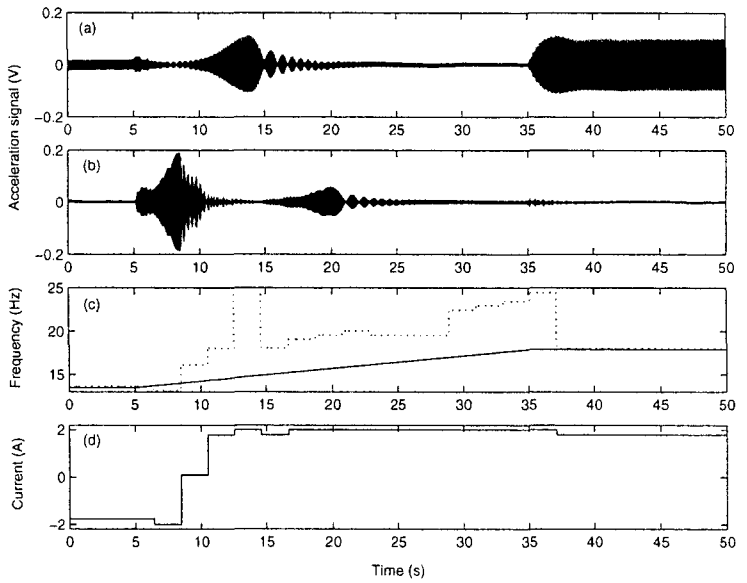

Figure 2.21: Experimental results for the linear change of the exciting frequency, N=2048 and using Eq. (2.6): (a) response of the primary mass without control of EMVA; (b) response of the primary mass with control of EMVA; (c) the exciting frequency (solid) and the measured frequency (dotted); (d) coil current.

In order to compare the difference of the performance of the EMVA when different data lengths are used for FFT, the experiments were conducted once more by setting $N = 1024$, so now the reaction time for tuning was 1.024 s. Further, for the three types of the exciting frequency variations, the current-frequency Eqs. (2.5) and (2.6) were applied respectively, and the experimental results were plotted in Fig. 2.22 - Fig. 2.27. It shows that both the data lengths $N = 1024$ or 2048 used in FFT can provide a similar performance in vibration suppression.

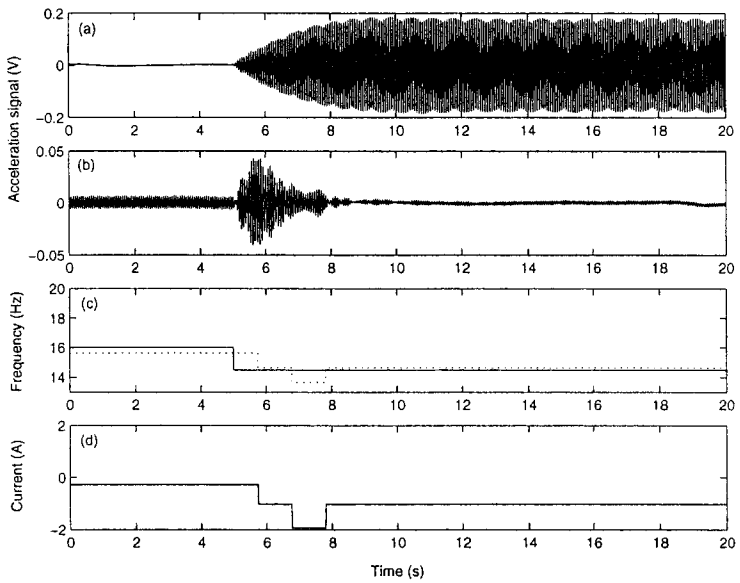

Figure 2.22: Experimental results for one step change of the exciting frequency, N=1024 and using Eq. (2.5): (a) response of the primary mass without control of EMVA; (b) response of the primary mass with control of EMVA; (c) the exciting frequency (solid) and the measured frequency (dotted); (d) coil current.

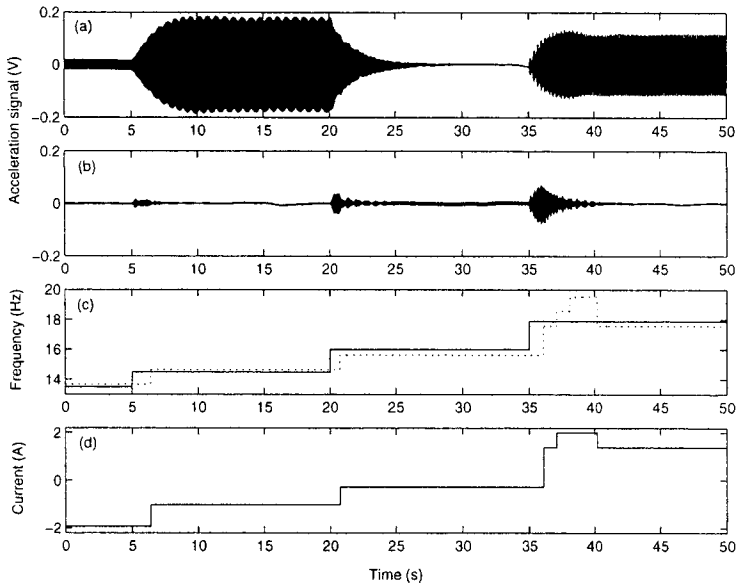

Figure 2.23: Experimental results for multi-step change of the exciting frequency, N=1024 and using Eq. (2.5): (a) response of the primary mass without control of EMVA; (b) response of the primary mass with control of EMVA; (c) the exciting frequency (solid) and the measured frequency (dotted); (d) coil current.

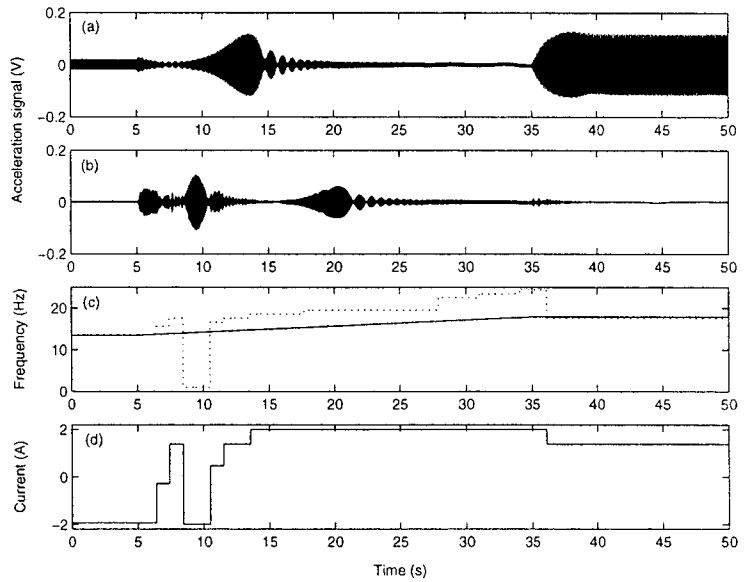

Figure 2.24: Experimental results for the linear change of the exciting frequency, N=1024 and using Eq. (2.5): (a) response of the primary mass without control of EMVA; (b) response of the primary mass with control of EMVA; (c) the exciting frequency (solid) and the measured frequency (dotted); (d) coil current.

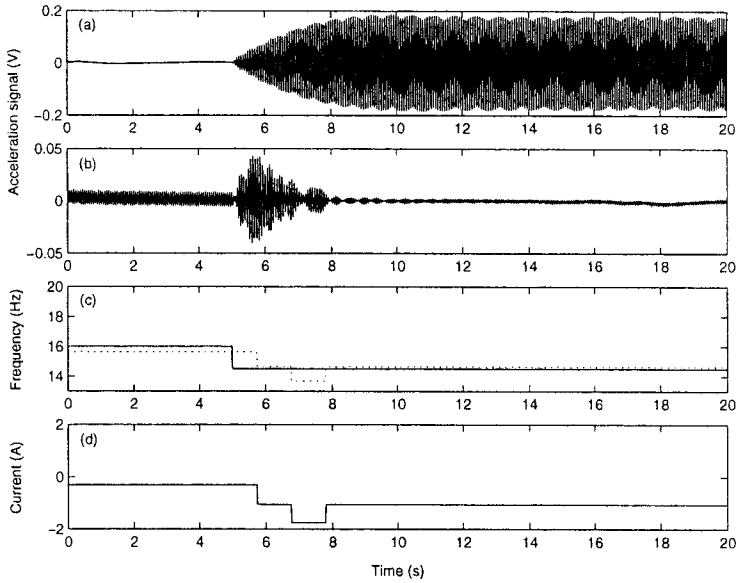

Figure 2.25: Experimental results for one step change of the exciting frequency, N=1024 and using Eq. (2.6): (a) response of the primary mass without control of EMVA; (b) response of the primary mass with control of EMVA; (c) the exciting frequency (solid) and the measured frequency (dotted); (d) coil current.

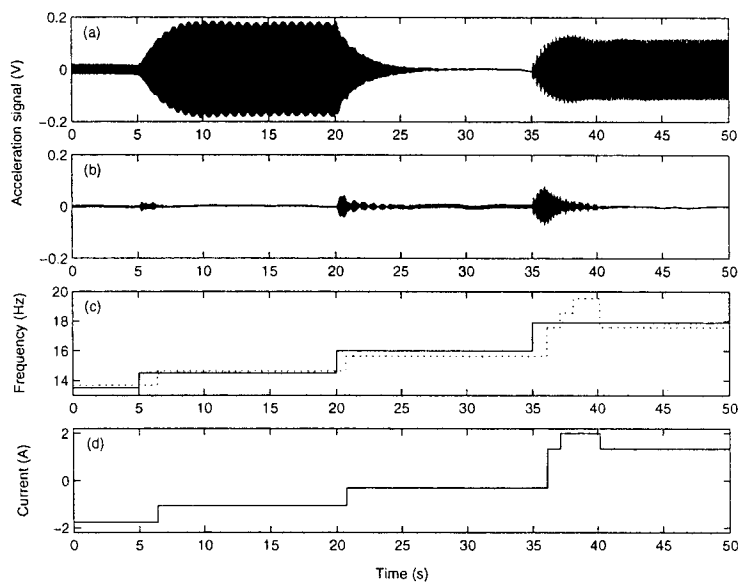

Figure 2.26: Experimental results for multi-step change of the exciting frequency, N=1024 and using Eq. (2.6): (a) response of the primary mass without control of EMVA; (b) response of the primary mass with control of EMVA; (c) the exciting frequency (solid) and the measured frequency (dotted); (d) coil current.

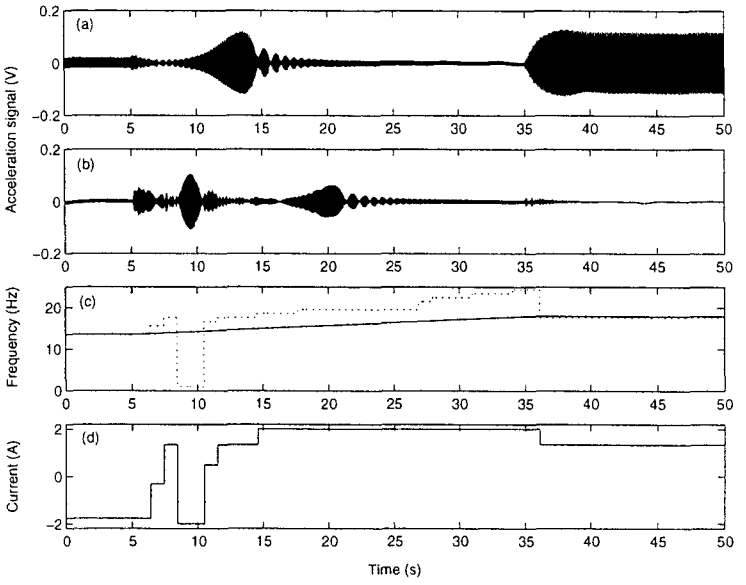

Figure 2.27: Experimental results for the linear change of the exciting frequency, N=1024 and using Eq. (2.6): (a) response of the primary mass without control of EMVA; (b) response of the primary mass with control of EMVA; (c) the exciting frequency (solid) and the measured frequency (dotted); (d) coil current.

Chapter 3

Several Design Issues on the EMVA

The current experimental setup has demonstrated the feasibility of the EMVA and its impressive effectiveness in vibration control; normally, the availability of the materials and/or the complexity of the experimental procedure often impose the constrains or limitations on the design; however, it is possible to extend the research in theory. This chapter examines and addresses several design issues related to the EMVA. First, a simplified equation is proposed to compute the flux density distribution in the gap of the electromagnet, and the approximation error caused by this simplification is investigated. Second, the effect of cross-sectional shapes of the permanent magnet on the variable magnetic stiffness and the constant magnetic stiffness is examined. Finally, how the gap spaces of the electromagnet affect the variable magnetic stiffness k_v is studied.

3.1 A Simplified Equation for the Determination of the Flux Density of the Electromagnet

To determine the magnetic stiffness caused by the interaction between the permanent magnet and the electromagnet, first the magnetic field between the poles of te electromagnet needs to be found. In Chapter 1, it was done by using the fundamental theory of electromagnetism. It involves numerically solving a triple integration. In what follows, a simplified numerical approach is proposed and the approximation errors caused by this simplification are investigated.

The solution of Eq. (1.6) involves a triple integration which must be done numerically (note that finding E_1, E_2 requires one integration). To simplify the computation, the hollow cylinder may be replaced by a current carrying cylindrical sheet with a radius R. This way, Eq. (1.6)

becomes

$$B_{sz} = \int_0^L B_{lz}(R, r, z + \lambda) d\lambda \tag{3.1}$$

The loop current i should be substituted by

$$i = \frac{NI}{L} \tag{3.2}$$

Note that the flux density B_{sz} computed by Eq. (1.6) or Eq. (3.1) is the one without the effect of the core of the electromagnet. A ferromagnetic core can significantly magnify the magnetic strength. The effect is included by considering the relative permeability of the steel core and the flux leakage of the circuit.

With the flux density from one pole of the electromagnet available, the total magnetic flux densities B_z between the two poles of the electromagnet can then be found by superposition. Using the parameters given in Table 1.1 and I=1.5A, Fig. 3.1 shows a comparison of the result based on Eq. (1.6) and that based on Eq. (3.1). To use Eq. (3.1), the radius R is determined by

$$R = \sqrt{\frac{R_1^2 + R_2^2}{2}} \tag{3.3}$$

This R divides the cylinder into two cylinders that have the same cross-sectional areas. It can be seen that both Eqs. (1.6) and (3.1) give a similar distribution. To quantitatively compare the difference of the two results, an error index is defined as

$$\varepsilon = \sum_{i=1}^{51} \sum_{j=1}^{21} \left| B_z^1(r_i, z_j) - B_z^2(r_i, z_j) \right| \Big/ \sum_{i=1}^{51} \sum_{j=1}^{21} \left| B_z^1(r_i, z_j) \right| \tag{3.4}$$

where B_z^1 is the total flux density based on Eq. (1.6), B_z^2 the one based on Eq. (3.1), z_j is varied from 0 to .02 m in a step of .001 m and r_i is varied from 0 to .05 m in a step of .001 m. The following five cases are considered: (1) R_1=0.015 m, R_1=0.017 m, (2) R_1=0.014 m, R_1=0.018 m, (3) R_1=0.011 m, R_1=0.020 m, (4) R_1=0.009 m, R_1=0.021 m, (5) R_1=0.006 m, R_1=0.022 m. Note that the five cases are chosen in a way such that R=0.0161 m and $R_2 - R_1$ is increased. Fig. 3.2 compares the results in two ways. Fig. 3.2(a) gives $B_z^1 - B_z^2$ where B_z^1 corresponds to case three. Fig. 3.2(b) shows the error index ε for the five cases. It is noted that the error mainly occurs at the pole faces and in the radial direction around the radius R and the error increases with the increase of $R_2 - R_1$.

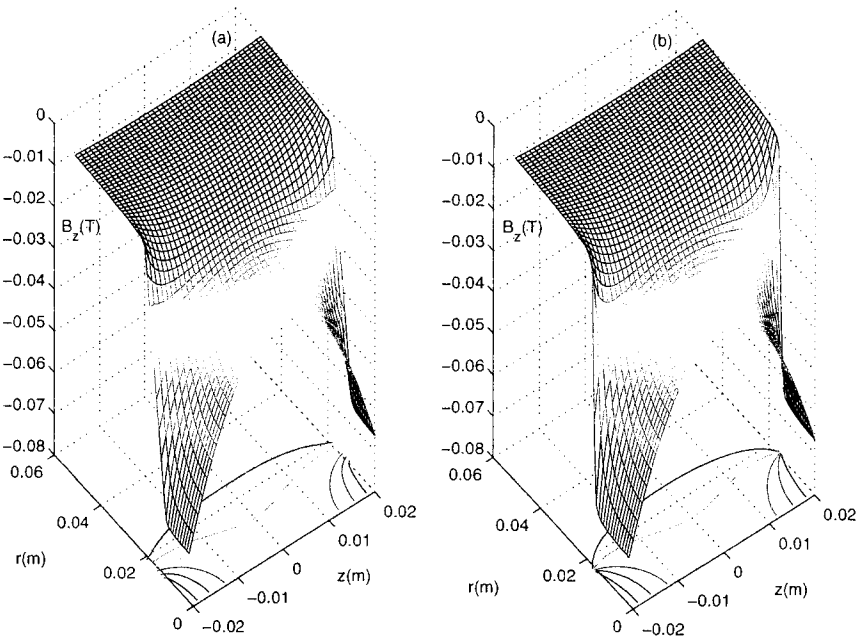

Figure 3.1: The magnetic flux density of the electromagnet for I = 1.5 A: (a) based on Eq. (1.6); (b) based on Eq. (3.1).

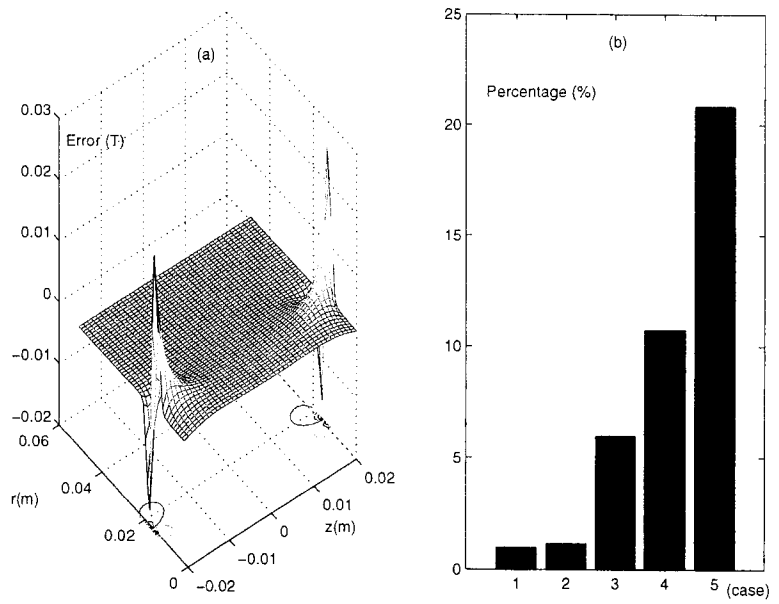

Figure 3.2: Comparison of B_z^1 and B_z^2; (a) $B_z^1 - B_z^2$; (b) ε defined by Eq. (3.4).

3.2 Effect of Different Cross-Sectional Shapes of PM on k_v

The present EMVA uses a rectangular shape PM because it is readily available. A natural question arises: how does a cross-sectional shape of the PM affect k_v ? To understand it, the interacting forces are computed using two more cross-sectional shapes: square and round. In the both cases, the dimension is chosen such that all the three cross sections have the same area. The magnetic field induced by the electromagnet is calculated using Eq. (1.8). Figure 3.3 compares the interaction forces versus displacement for these three cases. It is noted that the PM with a round shape offers the largest force variation, thus the largest stiffness while the PM with the rectangular shape offers the smallest force variation, thus the smallest stiffness.

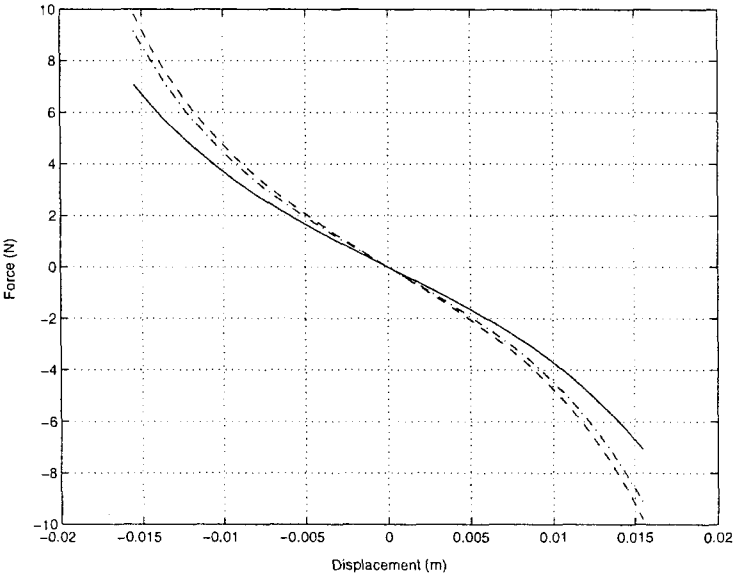

Figure 3.3: Interaction force versus the displacement of the PM for three different shapes of the PM: solid line, rectangular; dashdot line, square; dashed line, round.

3.3 Effect of Different Cross-Sectional Shapes of PM on k_{c2}

If the cross-sectional shape of the PM changes, it is expected that it will affect k_{c2}. Once again, consider the square shape PM and the round shape PM used above. The flux density from a square shape PM can be found by Eq. (1.13) with $w = l$. Following the derivation procedure given in [22], the equation for the flux density from a round shape PM is obtained as

(see Appendix A)

$$B_{pm} = \frac{\mu_0 M}{2}\left[\frac{z+h}{\left[r_{pm}^2+(z+h)^2\right]^{1/2}} - \frac{z}{\left[r_{pm}^2+z^2\right]^{1/2}}\right] \tag{3.5}$$

where r_{pm} is the radius of the PM. Using Eq. (1.15) with $\alpha = 0.913 \times 10^6\, mH^{-1}$, the interacting force between the PM and the core can be obtained. Figure 3.4 shows a comparison of the interacting forces caused by these three different shapes of the PMs. It is noted that the round shape results in the largest change in the force, thus the largest k_{c2} while the rectangular shape results in the smallest force variation, thus the smallest k_{c2}. It is also noted that the curve for the round shape PM appears more linear.

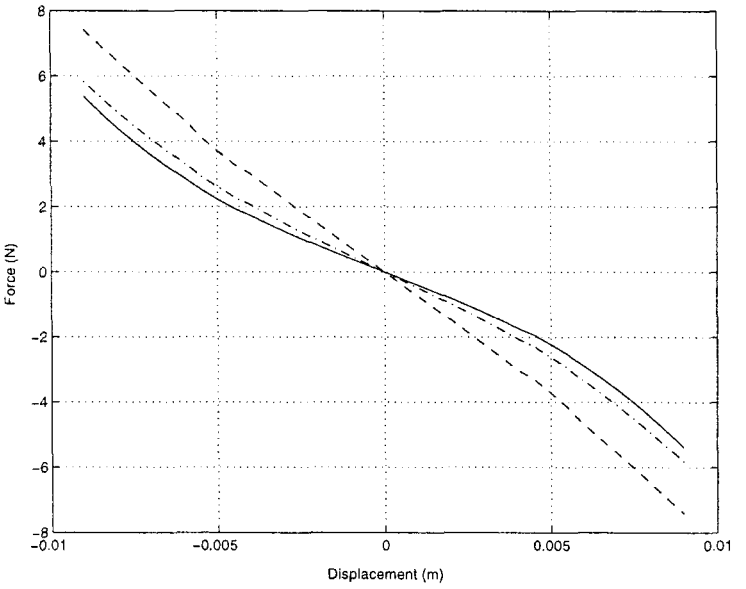

Figure 3.4: Interaction force of the PM and the core for three different shapes of PM: solid line, rectangular; dashdot line, square; dashed line, round.

3.4 Effect of the Gap Spaces of the Electromagnet on k_v

Consideration of the gap space of the electromagnet is based on several factors: the thickness of the PM, the maximum allowable displacement of the PM, and the size of the electromagnet, etc. With all the other parameters unchanged, two more gap spaces are considered. The interacting forces between the electromagnet and the PM for these three different gap spaces are shown in Fig. 3.5. It can be seen that with a narrower gap space, a greater and more linear stiffness k_v can be obtained.

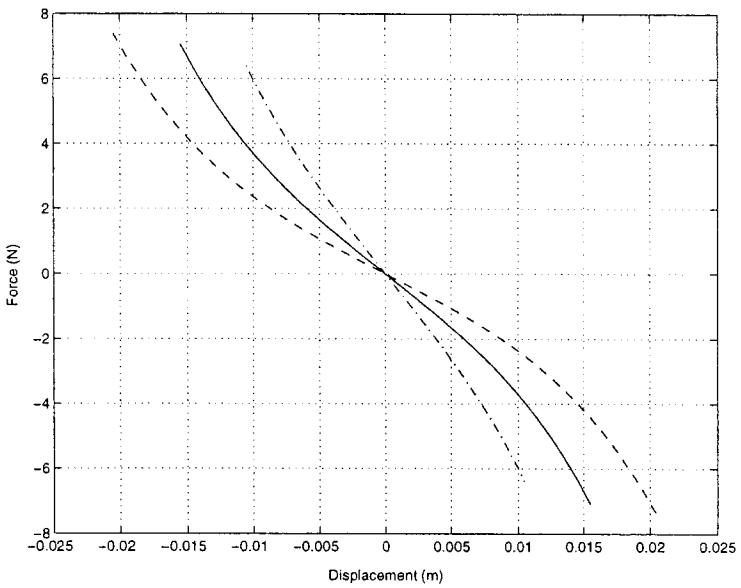

Figure 3.5: Interacting force between the electromagnet and the PM for three different gap spaces: solid line, δ=0.042 m; dashdot line, δ=0.032 m; dashed line, δ=0.052 m.

Part II

A TIME-DELAYED VIBRATION ABSORBER

Chapter 4

A Time-Delayed Vibration Absorber

4.1 Introduction

Excited by a harmonic disturbance, the primary structure will vibrate at the frequency of the driving force in the steady state. Traditionally, a passive absorber will be resorted to largely suppress this vibration in the event of the constant exciting frequency and the low damping in the system; however, when the driving frequency is shifting and/or there exists a high damping, it becomes impossible to bring the steady-state vibrations to rest or even to a desired small value only using a passive vibration control system; instead, the semi-active or active vibration control systems were being studied for decades, aiming to achieve better results in vibration suppression.

The time-delayed vibration absorber discussed in the second part of this thesis belongs to the family of the active control systems. In general, the active vibration control systems will apply dynamic forces at the same frequency of the primary excitation and can provide superior performance. The control forces within an active control system are typically generated by electro-hydraulic or electromechanical actuators based on the feedback information from the measured response of the structure and/or feedforward information from the external excitation. Its versatility and adaptability have been attracting considerable research interests in the vibration control area. The control system of an active dynamic vibration absorber was designed using the theory of output regulation with internal stability [15]. The subsequent experiment showed that vibration of the primary mass can be reduced to essentially zero at the specified frequency. In [17], the vibration suppression of a sinusoidally excited beam was well accomplished through the feedforward control of the alternating electric current, which subsequently generated the elec-

tromagnetic force on the electric line over the beam breadth. It was experimentally confirmed that the resonant oscillations of the first few modes could be well actively damped. In [24]-[25], an active vibration absorber was employed to entirely remove the internal damping of the device, hence increasing the attenuation of the host structure. A purely active vibration control of an elastic plate using piezoelectric actuators and sensors was reported in [26], and the H_2 control technique was applied for the controller design.

Dr. Nejat Olgac and his research group have been focusing on a novel active vibration absorption technique, the delayed resonator and its applications for more than a decade [27]-[32]. The delayed resonator can be considered to be a passive-active device that can work either passively or actively. In its passive mode, the device is a traditional vibration absorber. In its active mode, a controllable dynamic force is used to establish the internal resonance. Different from the foregoing literatures, this study presents a new perspective on the delayed resonator by examining its relationship with a traditional Proportional and Derivative (PD) controller. The study focuses on an inherent problem of such control technique: a conflicting goal of achieving the marginal stability of the absorber system and the stability of the combined system. To tackle this problem, an online tuning algorithm is proposed. An electromagnetic actuator is developed to test the tuning algorithm. The rest of this chapter is organized as follows: in Section 4.2, the delayed resonator is introduced from a viewpoint of a PD controller; in Section 4.3, the stability issue is discussed and the simulation results are presented; finally, in Section 4.4, the relationships between c, c_a, ω and the gain pairs g_c, g are studied.

4.2 The Time-Delayed Control System

Fig. 4.1 shows a primary system attached with a passive/active vibration absorber where m and m_a are the masses, c and c_a the damping values, k and k_a the stiffnesses of the primary system and the absorber system, respectively, $F_0 \sin(\omega t)$ an external harmonic excitation, ω the exciting frequency, and u the actuating force. Note that when $u = 0$, the absorber becomes a passive one. The passive vibration absorber is suitable when the external disturbance is a single harmonic force with a fixed frequency and the damping value c_a is low. However, when the exciting frequency varies or the absorber damping is high, the performance of the passive absorber deteriorates. The equation of motion of the system is given by

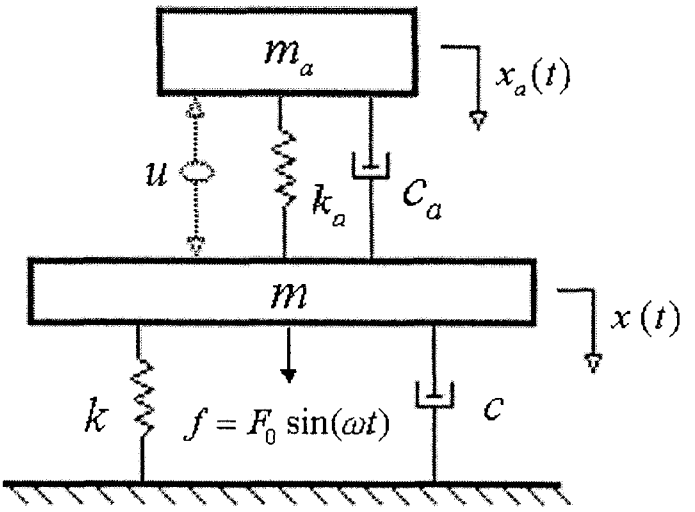

Figure 4.1: The system with a passive/active vibration absorber.

$$\begin{bmatrix} m & 0 \\ 0 & m_a \end{bmatrix} \begin{bmatrix} \ddot{x}(t) \\ \ddot{x}_a(t) \end{bmatrix} + \begin{bmatrix} c + c_a & -c_a \\ -c_a & c_a \end{bmatrix} \begin{bmatrix} \dot{x}(t) \\ \dot{x}_a(t) \end{bmatrix} + \begin{bmatrix} k + k_a & -k_a \\ -k_a & k_a \end{bmatrix} \begin{bmatrix} x(t) \\ x_a(t) \end{bmatrix} = \begin{bmatrix} F_0 \sin(\omega t) + u \\ -u \end{bmatrix} \tag{4.1}$$

Despite the abundance of the sophisticated tools, including the advanced controllers, the Proportional-Integral-Derivative (PID) controller is still most widely used in modern industry, controlling more than 95% of closed-loop industrial processes because of its simplicity and versatility. The PID controller has been proven to be robust and effective in many important control applications. In this study, a PD controller is developed with the state feedback from the absorber mass. The control effort is given as

$$u(t) = k_p x_a(t) + k_d \dot{x}_a(t) \tag{4.2}$$

Let the steady-state displacements of the primary mass and absorber mass be of the form

$$x(t) = Xe^{j\omega t}, x_a(t) = X_a e^{j\omega t} \tag{4.3}$$

where $j = \sqrt{-1}$. Substitution of these steady-state forms into Eq. (4.1) yields the steady-state

displacement amplitude of the primary mass,

$$X = \frac{(k_p + k_a - m_a\omega^2) + j(c_a + k_d)\omega}{\begin{vmatrix} k + k_a - m\omega^2 + j(c + c_a)\omega & -(k_a + k_p) - j(c_a + k_d)\omega \\ -k_a - jc_a\omega & k_a + k_p - m_a\omega^2 + j(c_a + k_d)\omega \end{vmatrix}} F_0 \tag{4.4}$$

It can be seen that setting the numerator of Eq. (4.4) to be zero can bring the steady-state displacement of the primary mass to rest, i.e.,

$$(k_p + k_a - m_a\omega^2) + j(c_a + k_d)\omega = 0 \tag{4.5}$$

or

$$k_p = m_a\omega^2 - k_a, k_d = -c_a \tag{4.6}$$

When the conditions represented by Eq. (4.6) are satisfied, the vibrations of the primary system will be suppressed completely in the steady state. It is important to point out that the traditional PD controller needs two states feedback to operate, the displacement and the velocity, which often imposes limitation on most users when only one kind of sensor is available, now a question arises if the PD control algorithm can be modified so that only one state feedback is necessary for the operation. In the specific case that the excitation is a sinusoidal force, the displacement, the velocity and the acceleration of either the absorber mass or the primary mass have a certain mathematical relationship in the steady state:

$$x_a(t) = \dot{x}_a(t - T/4)/\omega, x_a(t) = \ddot{x}_a(t - T/2)/\omega^2 \tag{4.7}$$

where $T = 2\pi/\omega$ is the period of the exciting force. Utilizing the relationships in Eq. (4.7), the PD control effort can be modified to

$$u = k_p x_a(t) + k_d \dot{x}_a(t) = k_p x_a(t) + k_d \omega x_a(t + T/4) \tag{4.8}$$

Since the displacement $x_a(t)$ of the absorber mass is a sinusoidal wave, the control effort can be further expressed as

$$u = k_p x_a(t) - k_d \omega x_a(t - T/4) \tag{4.9}$$

Then, substituting Eq. (4.6) into Eq. (4.9) yields

$$u = (m_a\omega^2 - k_a)x_a(t) + (c_a\omega)x_a(t - T/4) \tag{4.10}$$

Equation (4.10) can be interpreted by a geometric representation as shown in Fig. 4.2, where $(m_a\omega^2 - k_a)x_a(t)$ is a vector with an angle ωt with respect to the horizontal axis and, $(c_a\omega)x_a(t - T/4)$ is a vector that is 90° lag of $(m_a\omega^2 - k_a)x_a(t)$. Note that $c_a\omega$ is certainly a positive number, but $m_a\omega^2 - k_a$ may be a negative or positive value; no matter which case it drops, these two vectors can always be represented by a new vector given as $gx_a(t - t_d)$ where

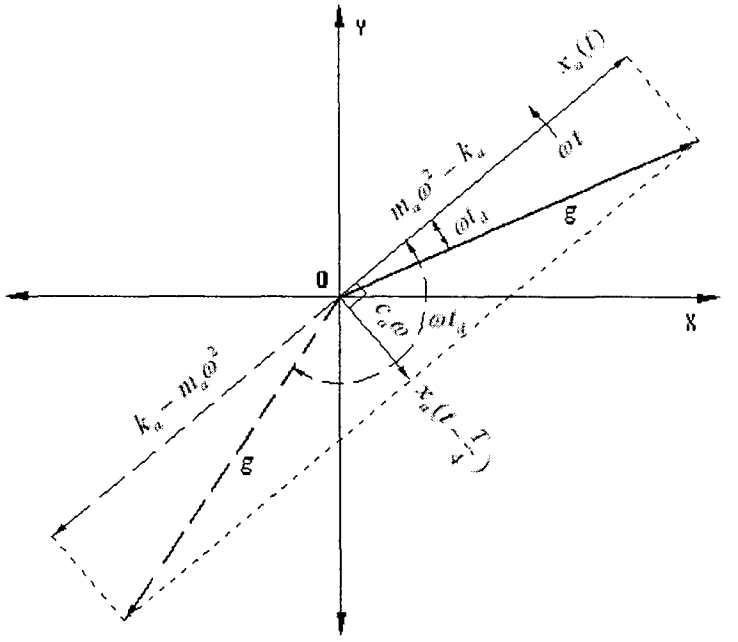

Figure 4.2: Vector representation of the control effort.

$$g = \sqrt{(m_a\omega^2 - k_a)^2 + (c_a\omega)^2} \tag{4.11}$$

$$t_d = \frac{1}{\omega}[\tan^{-1}(\frac{\omega c_a}{m_a\omega^2 - k_a}) + 2n\pi], n = 0, 1, 2, \ldots \tag{4.12}$$

Not surprisingly, Eqs. (4.11) and (4.12) give the gain and the delay time, respectively, of the delayed resonator proposed by Dr. Olgac [27]. Now Eq. (4.10) becomes

$$u = gx_a(t - t_d) \tag{4.13}$$

The proportional time-delayed control system designed above is a partial state feedback one. It makes use of only one state element: the displacement of the absorber. This feature will facilitate the implementation in case that only one type of sensor is available. It is worth mentioning that any of the other two state elements, the velocity or the acceleration, may be

used to realize the time-delayed controller as well, their corresponding gains and time-delays are calculated by the following equations, respectively (refer to Eq. (4.7)): with a delayed velocity feedback

$$g = \frac{1}{\omega}\sqrt{(m_a\omega^2 - k_a)^2 + (c_a\omega)^2} \tag{4.14}$$

$$t_d = \frac{1}{\omega}[\tan^{-1}(\frac{\omega c_a}{m_a\omega^2 - k_a}) + (2n + 0.5)\pi], n = 0, 1, 2, \ldots \tag{4.15}$$

Or with a delayed acceleration feedback

$$g = \frac{1}{\omega^2}\sqrt{(m_a\omega^2 - k_a)^2 + (c_a\omega)^2} \tag{4.16}$$

$$t_d = \frac{1}{\omega}[\tan^{-1}(\frac{\omega c_a}{m_a\omega^2 - k_a}) + (2n + 1)\pi], n = 0, 1, 2, \ldots \tag{4.17}$$

Note the errors in Eq. (4) of [31]. The equations above demonstrate that, for a given passive vibration absorber system and a constant exciting frequency, the feedback gain is a fixed value; while, the time delay is multi-valued, it depends on which cycle is preferred for the signal feedback. It is also worth mentioning that the bigger time delay may lead to a slower reaction of the actuator.

4.3 Stability of the Combined System

The time-delayed vibration control system may introduce some unstable poles into the combined system, hence the stability issue arises. With the parameters designed for the controller, the characteristic equation of the entire 2-DOF system is given by

$$CE(s) = (m_a s^2 + c_a s + k_a)(ms^2 + cs + k) + m_a s^2(c_a s + k_a) + g_g s^l e^{-t_d s}(ms^2 + cs + k) = 0 \tag{4.18}$$

where g_g is the feedback gain of the global system and, $l = 0$ is for the displacement feedback, $l = 1$ for the velocity feedback and, $l = 2$ for the acceleration feedback, respectively. Equation (4.18) contains a time-delayed term; due to its transcendental nature, there should be infinitely many poles on the root loci for a fixed set of gain and time delay. Accordingly, there exist infinitely many poles on the imaginary axis, and each pole corresponds to a certain feedback gain which is referred to as the crossing gain in the literatures [27]-[28] and denoted as g_c in this study. The stability of the whole system is guaranteed only if the minimum crossing gain g_c is larger than the designed actuator gain g for the controller. In this case, the poles are located in the left half plane when the time-delayed active vibration absorber takes the designed gain;

hence the entire system is asymptotically stable. When $g_c > g$, there is a safety margin for g. When $g_c < g$, the ideal delayed resonator is unachievable if the stability of the combined system is maintained.

Use the parameters of the experimental system (see next section) as an example: $m = 3.451$ kg, $c = 32.9$ Ns/m, $k = 31067$ N/m, $m_a = 0.253$ kg, $c_a = 1.484$ Ns/m, $k_a = 2277$ N/m. It is easy to find that the two natural frequencies of the system are 13.1 Hz and 17.3 Hz, respectively. Assume that the disturbance frequency may take any value in the range of 5.0 Hz to 25 Hz. When the displacement signal of the absorber system is fedback, the designed actuator gain g can be obtained from Eq. (4.11); meanwhile, the minimum crossing gain g_c of the global system may be found using Eq. (4.18). The procedure for numerically obtaining g_c is given as follows: refering to [27], equation (4.18) can be further expressed as

$$CE(s) = A(s) + g_g e^{-t_d s} B(s) = 0 \tag{4.19}$$

where

$$\begin{aligned} A(s) &= (m_a s^2 + c_a s + k_a)(ms^2 + cs + k) + m_a s^2 (c_a s + k_a) \\ B(s) &= s^l (ms^2 + cs + k) \end{aligned} \tag{4.20}$$

with $l = 0$ for the displacement feedback, $l = 1$ for the velocity feedback and, $l = 2$ for the acceleration feedback. Let $s = j\omega_c$, where ω_c is the global crossing frequency corresponding to g_c, the following relations can be reached:

$$A(j\omega_c) = -g_c e^{-jt_d\omega_c} B(j\omega_c) \tag{4.21}$$

or

$$g_c e^{j(\pi - t_d\omega_c)} = \frac{A(j\omega_c)}{B(j\omega_c)} \tag{4.22}$$

The angular condition and the gain condition can then be derived respectively as

$$e^{j(\pi - t_d\omega_c)} = e^{j\left[\angle A(j\omega_c) - \angle B(j\omega_c)\right]} \tag{4.23}$$

$$g_c = \left| \frac{A(j\omega_c)}{B(j\omega_c)} \right| \tag{4.24}$$

Using the angular condition to find the crossing frequencies, and the corresponding crossing gains on the imaginary axis can be subsequently obtained. Pick out the minimum global crossing gain as g_c. When $\omega = 13.1$ Hz, for example, $t_d = 0.036$ s. For a certain exciting frequency ω, the

time delay t_d can be calculated. Vary ω_c to find a series of global crossing frequencies which satisfy the angular condition represented by Eq. (4.23), then the corresponding global gains can be derived from Eq. (4.24). Check the trend of the variation of g_c to find the minimum global crossing gain. Those gain pairs for different exciting frequencies were plotted in Fig. 4.3. It shows that the two curves intersect around 14 Hz. In the case of the exciting frequency below 14 Hz, $g_c < g$ holds, it implies that the feedback gain cannot take the designed value. When the exciting frequency is above 14 Hz, the condition $g_c > g$ exists; the ideal delayed control can be realized. It is understandable that the closer the achievable actuator gain approaches the designed gain g, the better performance the actuator can give. Fig. 4.4 illustrates the relationships between the designed actuator gain g, the time delay t_d and the exciting frequency ω (in Hz). It can be seen that increasing ω causes t_d to decrease, and drives g lower, and then it rises.

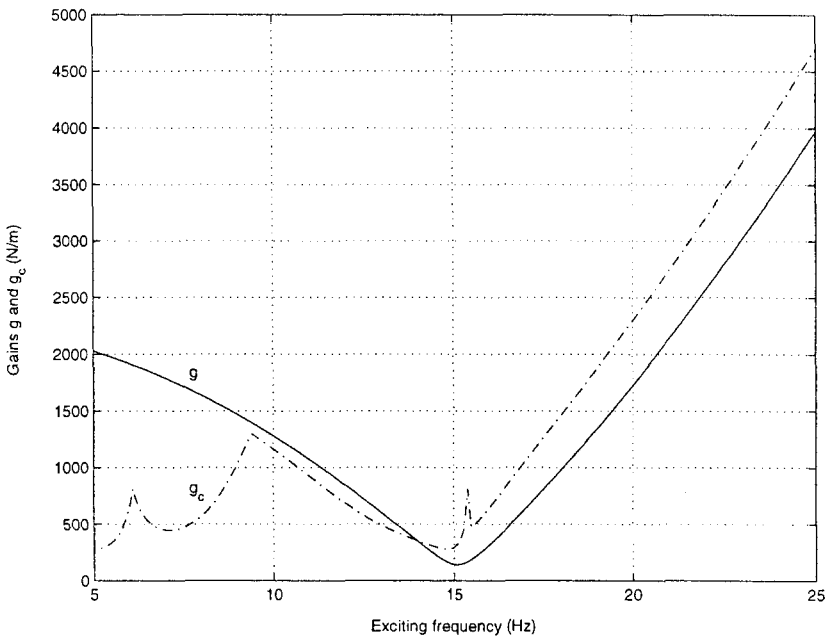

Figure 4.3: The designed gain g (solid) and the minimum crossing gain g_c (dash-dot) versus the exciting frequencies with the displacement feedback.

Numerical simulations were done when ω =17.3 Hz and 13.1 Hz, respectively. The feedback gains and the time delays of the actuator are 730 N/m and 0.002 s, 576 N/m and 0.036 s, respectively, as per Eqs. (4.11), (4.12). The results are plotted in Fig. 4.5. It validates two points: first, the actuator is capable of suppressing the vibration of the primary system to essentially zero

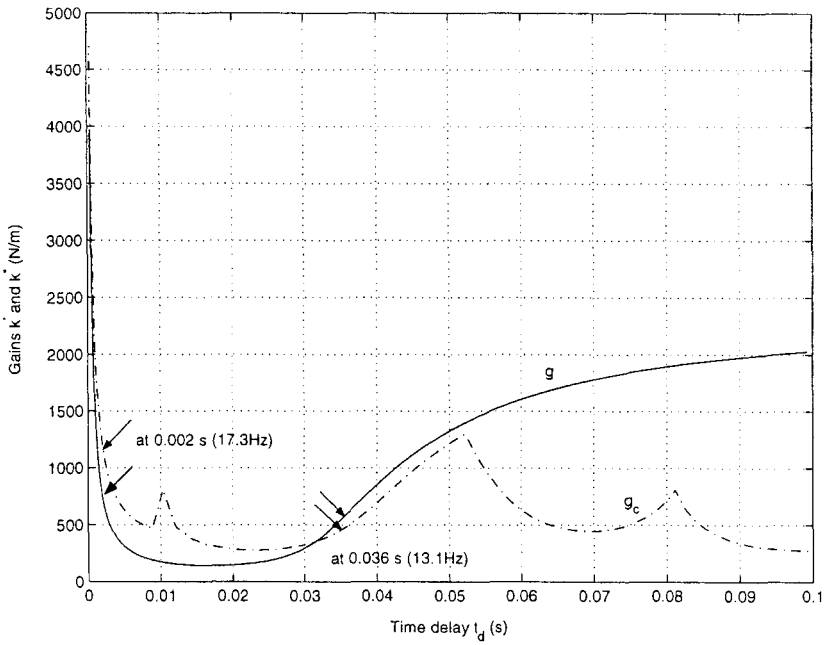

Figure 4.4: The designed actuator gain g (solid) and the minimum crossing gain g_c (dash-dot) of the global system versus the time delay t_d respectively when the exciting frequency ω is increasing (along the arrow).

at $\omega = 17.3$ Hz; second, the response of the primary system runs into the divergent instability with the designed actuator gain at $\omega = 13.1$ Hz.

The velocity or the acceleration signal can also be fedback to the actuator instead of the displacement. In such case, the stability analysis should be carried out following the similar procedure to the displacement feedback, based on Eq. (4.18). It is noted that, normally, the frequency range for the stability or instability of the system would be different for different types of state feedback. For instance, when the acceleration signal is used to activate the actuator in the current system, the stable frequency range dwindles to [14, 16.5] Hz, as shown in Fig. 4.6. Note that the feedback gain is a very small value, due to the large acceleration signal. In the unstable frequency range, the actuator may still work to some degree; under this circumstance, the maximum feedback gain should be smaller than the minimum crossing gain of the global system. Experiments in Chapter 5 will demonstrate the effectiveness of the time-delayed vibration control system with acceleration feedback at the two resonance frequencies, both of which drop in unstable frequency range. Correspondingly, Fig. 4.7 illustrates the relationships between the designed actuator gain g, the time delay t_d and the exciting frequency ω (in Hz) for the

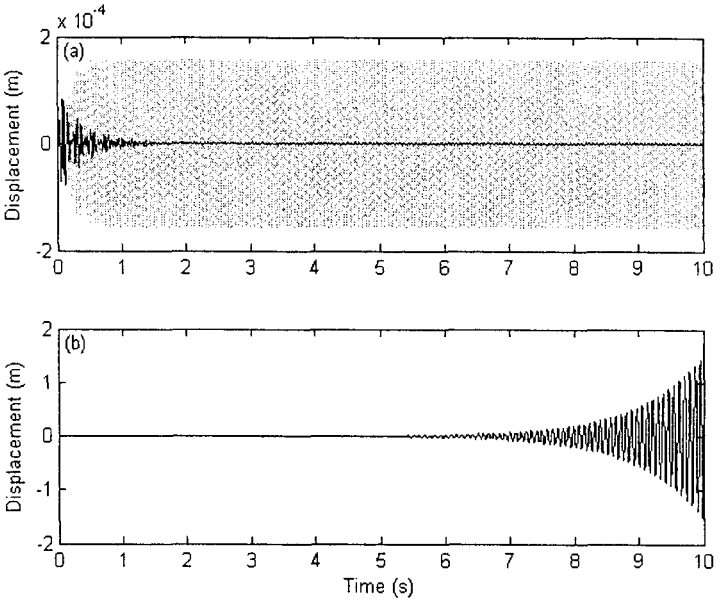

Figure 4.5: The response of the primary system: (a) ω =17.3 Hz; without control (gray); with control (dark); (b) ω =13.1 Hz; with control.

acceleration feedback.

4.4 Relationships between c, c_a, ω and the Gain Pairs g_c, g

The main concern on this type of time-delayed vibration absorber is that the designed actuator parameters may cause instability in the system at some frequency ranges. As expected, the damping values c and c_a play a significant role in the stability analysis of the global system. In order to better understand the relationships between c, c_a, ω and the gain pairs g_c, g, a number of numerical computations have been done, and the results were plotted in Figs. 4.8 - 4.11. Please note in the following figures, the damping ratios were used instead of the damping values, the relations between them are

$$\zeta = c/(2\sqrt{km}), \zeta_a = c_a/(2\sqrt{k_a m_a}) \tag{4.25}$$

Two types of output feedback have been considered: displacement feedback and acceleration feedback.

- Displacement Feedback: Figure 4.8 shows in the case that ζ is fixed and ζ_a is increasing, the intersection frequency corresponding to the condition of $g = g_c$, is increasing slightly as well;

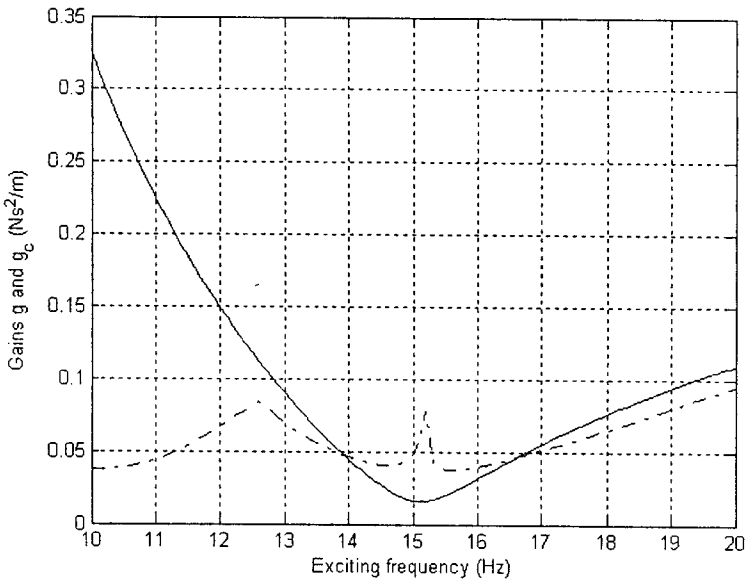

Figure 4.6: The designed actuator gain g (solid) and the minimum crossing gain g_c (dash-dot) of the global system versus the exciting frequencies with the acceleration feedback.

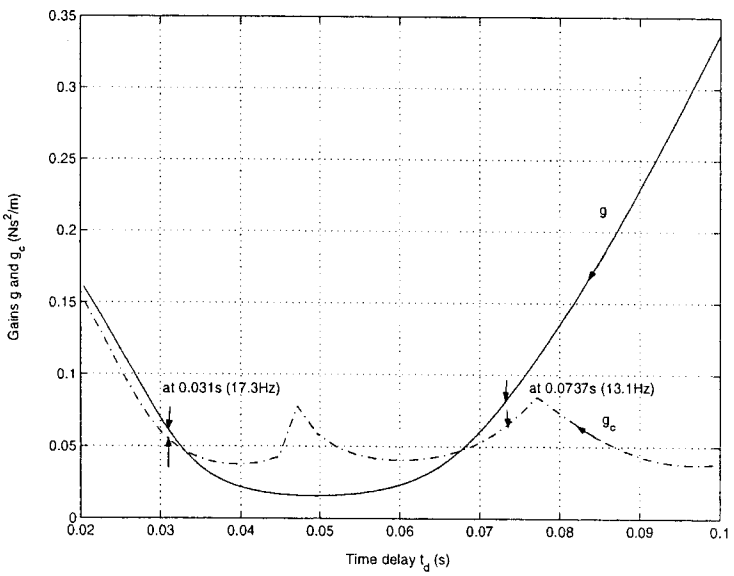

Figure 4.7: The designed actuator gain g (solid) and the minimum crossing gain g_c (dash-dot) of the global system versus the time delay t_d respectively when the exciting frequency ω is increasing (along the arrow).

for the exciting frequencies lower than that intersection frequency, it can be seen that the operable range, where g_c is close to g, becomes bigger; for the exciting frequencies above that intersection frequency, the adjustable margin for g, i.e., the gap between g_c and g, narrows. Correspondingly, Fig. 4.9 illustrates the relationships between the designed actuator gain g, the minimum global crossing gain g_c and the time delay t_d when the exciting frequency ω is increasing.

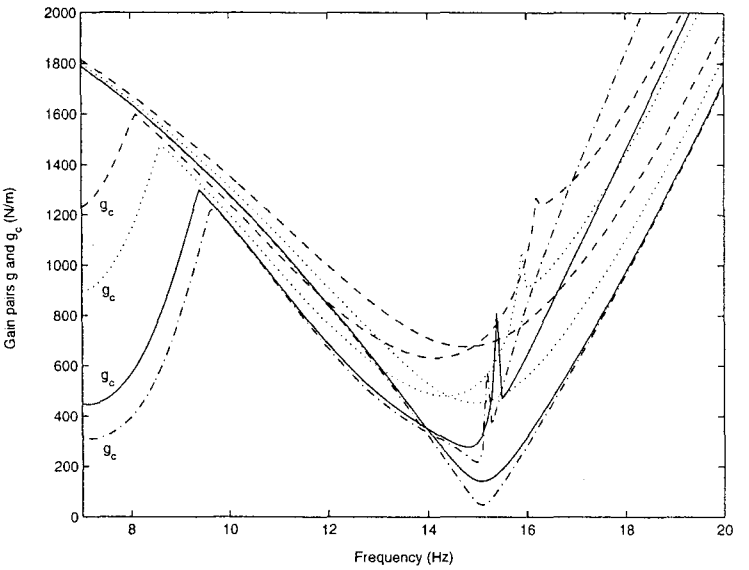

Figure 4.8: The designed gain g and the minimum crossing gain g_c versus the exciting frequencies with the displacement feedback; $\zeta = 0.05$ fixed, ζ_a changes: dashdot, ζ_a=0.01; solid, ζ_a=0.03; dotted, ζ_a=0.1; dashed, ζ_a=0.15;

Under the circumstance that ζ_a is fixed and ζ changes, it can be seen from Fig. 4.10 and Fig. 4.11 that all the curves for g versus the exciting frequency appear the same, regardless of the variations of c. This is because that the designed actuator gain g has nothing to do with the primary system, as per Eq. (4.11); however, the difference in the damping value c will lead to a different g_c.

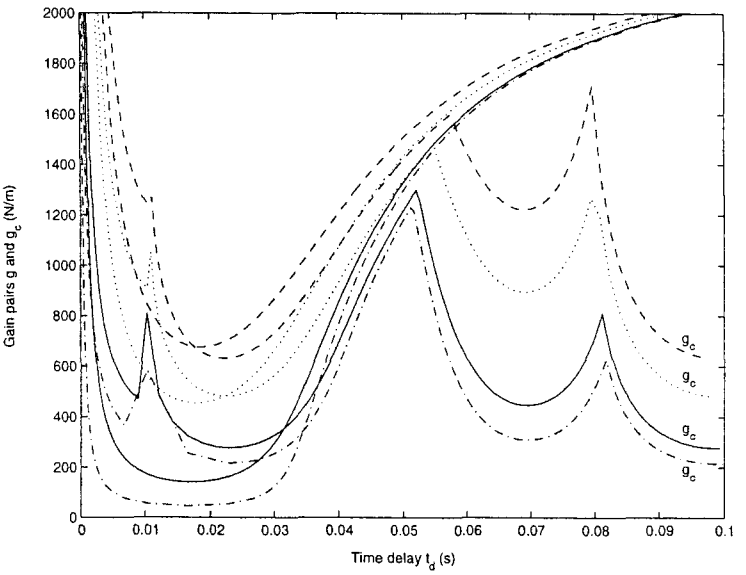

Figure 4.9: The designed gain g and the minimum crossing gain g_c versus the time delay t_d respectively when the exciting frequency ω is increasing from 5 Hz to 25 Hz; displacement feedback; $\zeta = 0.05$ fixed, ζ_a changes: dashdot, ζ_a=0.01; solid, ζ_a=0.03; dotted, ζ_a=0.1; dashed, ζ_a=0.15;

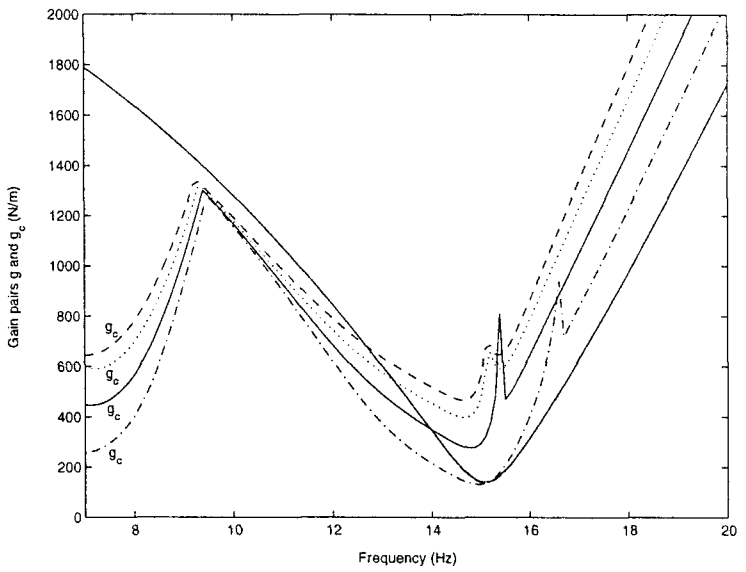

Figure 4.10: The designed gain g and the minimum crossing gain g_c versus the exciting frequencies with the displacement feedback; $\zeta_a = 0.03$ fixed, ζ changes: dashdot, ζ=0.01; solid, ζ=0.05; dotted, ζ=0.1; dashed, ζ=0.15;

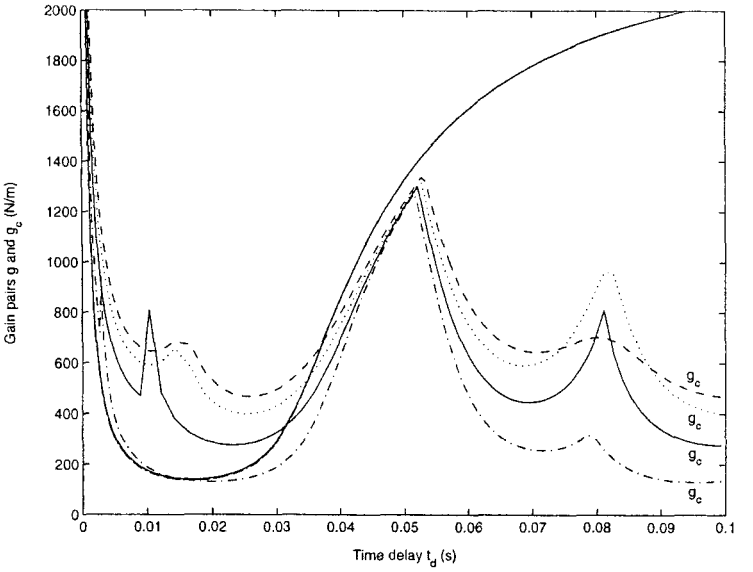

Figure 4.11: The designed gain g and the minimum crossing gain g_c versus the time delay t_d respectively when the exciting frequency ω is increasing from 5 Hz to 25 Hz; displacement feedback; $\zeta_a = 0.03$ fixed, ζ changes: dashdot, ζ=0.01; solid, ζ=0.05; dotted, ζ=0.1; dashed, ζ=0.15;

- Acceleration Feedback: Compared to the displacement feedback, the stability frequency range for the acceleration signal feedback is much smaller, limited only to the area around the anti-resonance frequency, which can be seen from Figs. 4.12 and 4.14; however, as the damping ratio grows, that stability range increases slightly. It implies that in most cases the designed actuator gain g is not achievable and, the maximum realizable gain to make the system stable is g_c.

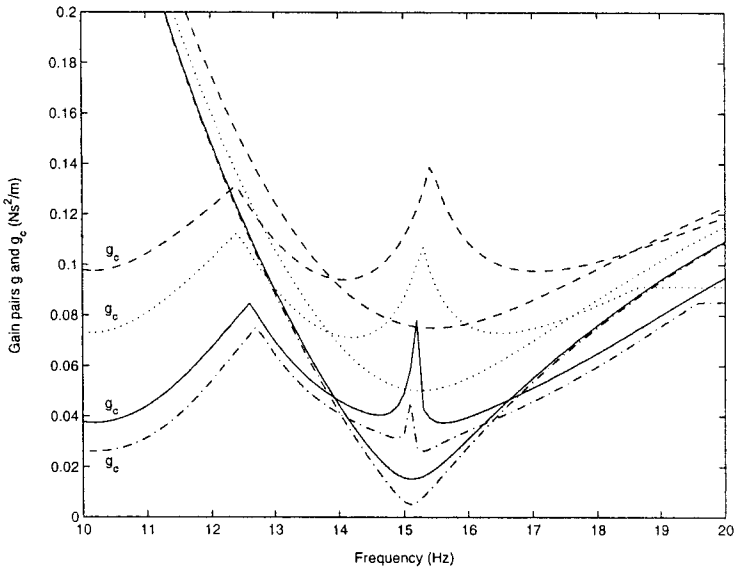

Figure 4.12: The designed gain g and the minimum crossing gain g_c versus the exciting frequencies with the acceleration feedback; $\zeta = 0.05$ fixed, ζ_a changes: dashdot, ζ_a=0.01; solid, ζ_a=0.03; dotted, ζ_a=0.1; dashed, ζ_a=0.15;

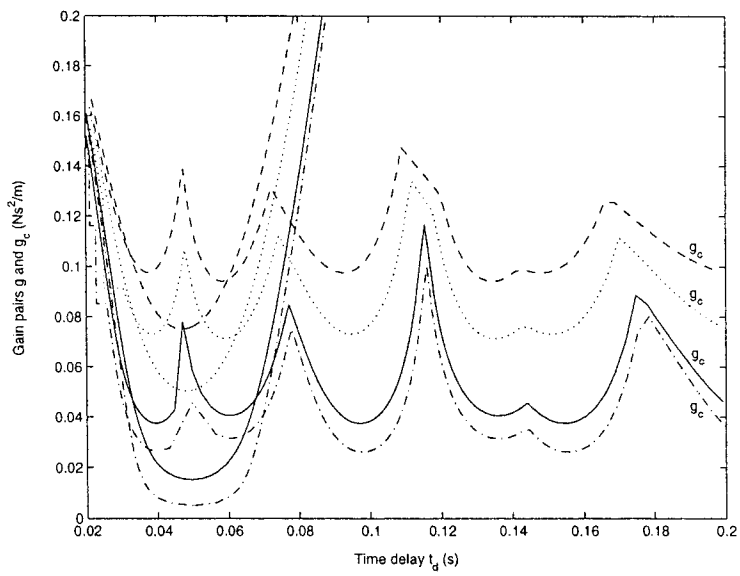

Figure 4.13: The designed gain g and the minimum crossing gain g_c versus the time delay t_d respectively when the exciting frequency ω is increasing from 5 Hz to 25 Hz; acceleration feedback; $\zeta = 0.05$ fixed, ζ_a changes: dashdot, ζ_a=0.01; solid, ζ_a=0.03; dotted, ζ_a=0.1; dashed, ζ_a=0.15;

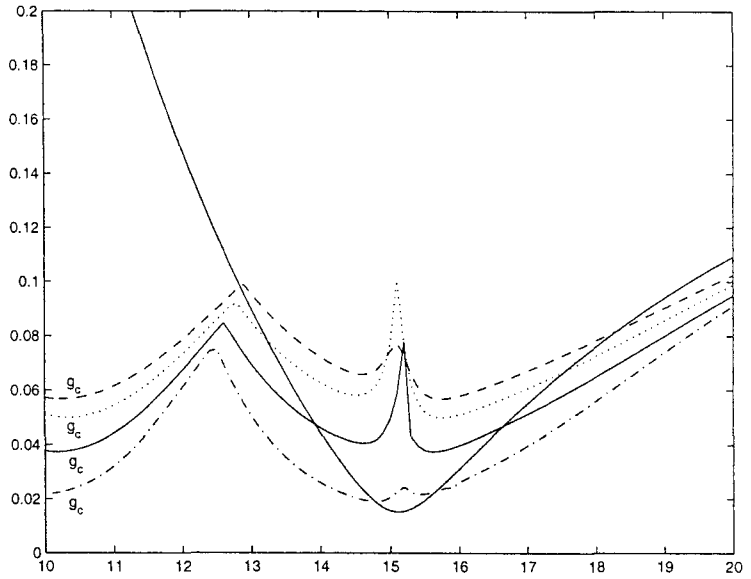

Figure 4.14: The designed gain g and the minimum crossing gain g_c versus the exciting frequencies with the acceleration feedback; $\zeta_a = 0.03$ fixed, ζ changes: dashdot, ζ=0.01; solid, ζ=0.05; dotted, ζ=0.1; dashed, ζ=0.15;

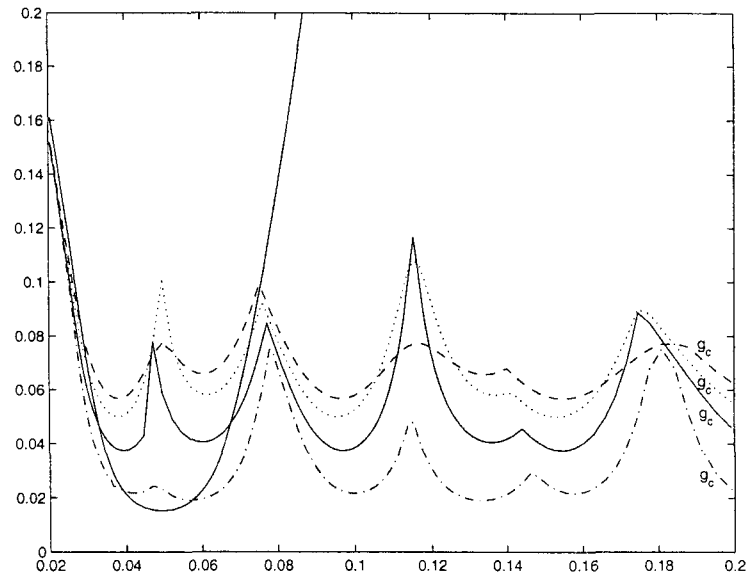

Figure 4.15: The designed gain g and the minimum crossing gain g_c versus the time delay t_d respectively when the exciting frequency ω is increasing from 5 Hz to 25 Hz; acceleration feedback; $\zeta_a = 0.03$ fixed, ζ changes: dashdot, ζ=0.01; solid, ζ=0.05; dotted, ζ=0.1; dashed, ζ=0.15;

Chapter 5

Experiment

This chapter presents the experimental results of the time-delayed vibration absorber. The chapter is organized as follows: an actuator was developed to realize the designed control algorithm of the time-delayed vibration control system. Subsequently, the experiment was conducted to validate its effectiveness in the vibration suppression.

5.1 The Experimental Setup

Fig. 5.1 shows a photograph of the developed time-delayed control system attached to a primary system. The entire experimental system consists of four subsystems: primary system, absorber system, actuator and computer control system. As schematically shown in Fig. 5.2, the absorber system comprises a clamped-clamped aluminum beam (1) and a permanent magnet (PM) (2) that is embedded in the center of the beam and placed between two electromagnets (3). The electromagnet is constructed by winding Gauge 22 copper wire around a steel core. The permanent magnet plays a dual role: acting as an absorber mass and forming an actuator to produce the proper control force by interacting with the electromagnets. The reason for replacing the C-shaped electromagnet in Part I with two new electromagnets is that the polarities of these two electromagnets at the ends close to the PM should be always kept the same, South or North simultaneously. The primary system (4) is an aluminum slab supported by an aluminum plate on each side, acting like a single degree-of-freedom (DOF) system. The electromagnets are fastened to the slab by two brackets, forming part of the primary mass. A small permanent magnet (5) is glued on an aluminum bar that is clamped to the primary mass. This permanent magnet interacts with an electromagnetic shaker (6) to generate a non-contact exciting disturbance. The

purpose of adding the aluminum bar between the permanent magnet and the primary mass is to minimize the interference of the magnetic field generated by the electromagnetic shaker and the one generated by the actuator. The mechanical properties of the system are given in Chapter 4, and the electrical properties of the actuator electromagnets are: L=150 mH, R=13 Ω. The computer control system is described as follows: the response of the absorber mass is measured by an accelerometer and conditioned via a charger amplifier. Subsequently, the Data Acquisition Board DS1102 (dSpace) is utilized to convert the signals from analog to digital or digital to analog. ControlDesk (dSpace) provides the interface between Matlab, Simulink and DS1102. A Simulink model depicted in Fig. 5.4 was developed to implement on-line optimum gain tracking, thus realize the time-delayed proportional state-feedback control algorithm. In the following step, a controlled alternating voltage is sent to the electromagnet windings through the current regulator board. Those two electromagnet windings are connected in parallel in the circuit. The exciting signal is generated by a subsystem within the Simulink model and sent to a power amplifier. The output of the amplifier drives the electromagnetic shaker to excite the primary system.

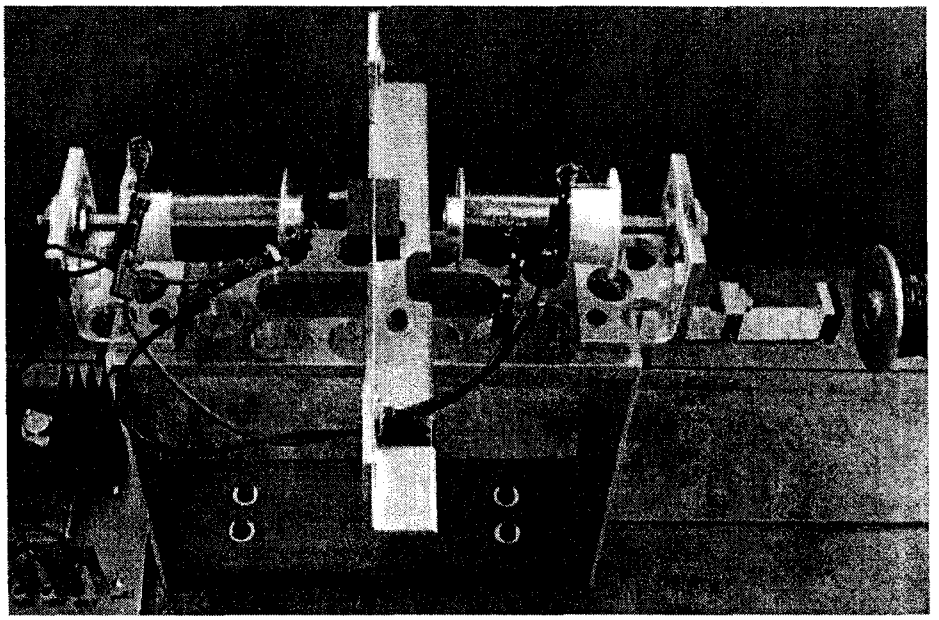

Figure 5.1: Photograph of the experimental setup.

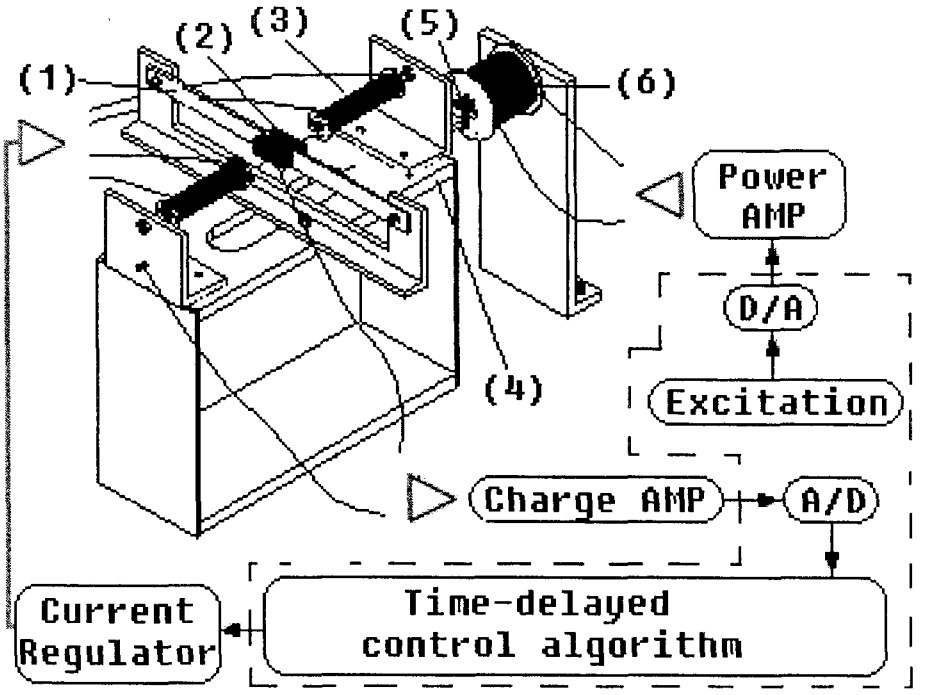

Figure 5.2: Schematic of the entire experimental system.

5.2 The Actuating Force

According to the control law of the time-delayed control system, a proper actuating force is desired to actively suppress the vibration of the primary system. This force can be produced by placing a permanent magnet at the gap center of two electromagnets. Assume that these two electromagnets have the same electrical characteristics and operate under the same conditions. The interaction force between the permanent magnet and one electromagnet is approximately proportional to the current flowing through its winding and inversely proportional to the square of the air gap, i.e.

$$F_1 = \lambda i / (G_{ap} - x_a)^2 \tag{5.1}$$

where λ is a constant related to the property of the actuator, i the winding current, G_{ap} the air gap when the permanent magnet is at its equilibrium position and, x_a the displacement of the permanent magnet. It should be noted that the force between an electromagnet and a steel surface is proportional to the square of the winding current. Correspondingly, the interaction

force between the permanent magnet and the other electromagnet is given by

$$F_2 = \lambda i \Big/ (G_{ap} + x_a)^2 \tag{5.2}$$

For the slight motion of the absorber mass about its equilibrium position, (As to the current setup, $G_{ap} = 26$ mm and, the maximum displacement magnitude of the absorber mass is around 6 mm.) the forces above can be approximated by the linear equations,

$$F_1 \approx \lambda i \Big/ G_{ap}^2 (1 + 2x_a/G_{ap}) \tag{5.3}$$

$$F_2 \approx \lambda i \Big/ G_{ap}^2 (1 - 2x_a/G_{ap}) \tag{5.4}$$

By controlling the phase of the alternating winding current, the forces F_1 and F_2 keep the same direction, thus the net electromagnetic actuating force on the permanent magnet is

$$F_{net} = F_1 + F_2 \approx 2\lambda i \Big/ G_{ap}^2 \tag{5.5}$$

It indicates that this net force, the control effort, is proportional to the winding current only, due to the mutual field compensations from these two electromagnets. In this way, the force F_{net} is easily controllable provided that the displacement magnitude of the absorber is relatively small.

5.3 Online Tuning Strategy

For a given electro-mechanical system, the inherent time delay includes two parts: t_{mc} and t_e, where t_{mc} is the delay caused by the computation and the reaction of the mechanical system and t_e is the delay caused by the induction of the electromagnetic coils. Define t_s as the delay set by the control algorithm, clearly,

$$t_s = t_d - t_{mc} - t_e \tag{5.6}$$

Also note that t_d is multi-valued; it is preferable to set t_d such that t_s is a positive value, but as small as possible. t_e may be calculated as

$$t_e = [\tan^{-1}(\omega L/R)] \Big/ \omega \tag{5.7}$$

In the meantime, t_{mc} can be found to be 0.041 s using Eq. (5.8),

$$t_{mc} = t_d - t_s - t_e \tag{5.8}$$

where the time delay t_s in the simulink model can be mannually adjusted to be found which can lead to the best performance of this active vibration absorber.

When the time delay t_s (thus t_d) is accurately determined for a certain frequency, the feedback gain can be gradually enlarged until a point, bigger than that, the vibration of the primary system will start increasing and/or the system will go to unstable. That point is the optimum gain which can be achieved by the current experiment setup. Two cases should be considered. First, when the minimum global crossing gain g_c is bigger than the designed absorber gain g, the optimum gain is g; second, in the case of $g_c < g$, the optimum gain should be g_c. A flow chart of the optimum gain tracking program is illustrated in Fig. 5.3. The program is executed in the following way: every 0.512 s, the program collects 512 acceleration data from the primary mass, with the sampling time 1 ms. Those 512 data will be separated into two groups, the first 256 data and the second 256 data. The ratio between the Root Mean Square (RMS) values of those two groups of acceleration signals can then be calculated. This ratio may be utilized to determine the trend of the response of the primary mass. If this ratio is below 1.01, it means that the response of the primary mass is not increasing, so enlarging the gain is recommended; when the ratio is bigger than the threshold 1.03, it implies that the magnitude of $\ddot{x}(t)$ is rising, the optimum gain is just stepped over. The rationale of the program is to increase the feedback gain step by step, while monitoring the acceleration magnitude of the primary system. If the acceleration magnitude is decreasing or remaining the same, the gain should be added more. Once the acceleration magnitude begins growing, reduce the gain a little bit and then keep it unchanged, since the system has just run into instability and/or the optimum gain has been stepped over. This optimum gain tracking program is effective for the present experimental system under an assumption: except the harmonic excitation, no other disturbance exists. The advantage of this online tuning strategy lies in the effort-saving on the derivation of the accurate equations from the control command to the exact control force. It is worth mentioning that those thresholds were found experimentally. Take the upper threshold 1.03 for example. If this threshold is too small, it will not compromise the fluctuation of the magnitude of $\ddot{x}(t)$ in the transient response; while, if this threshold is too big, the auto-tuning gain will continuously increase regardless of the fact that the system has been divergently unstable. The experimental results with different settings of this threshold were demonstrated in the next section.

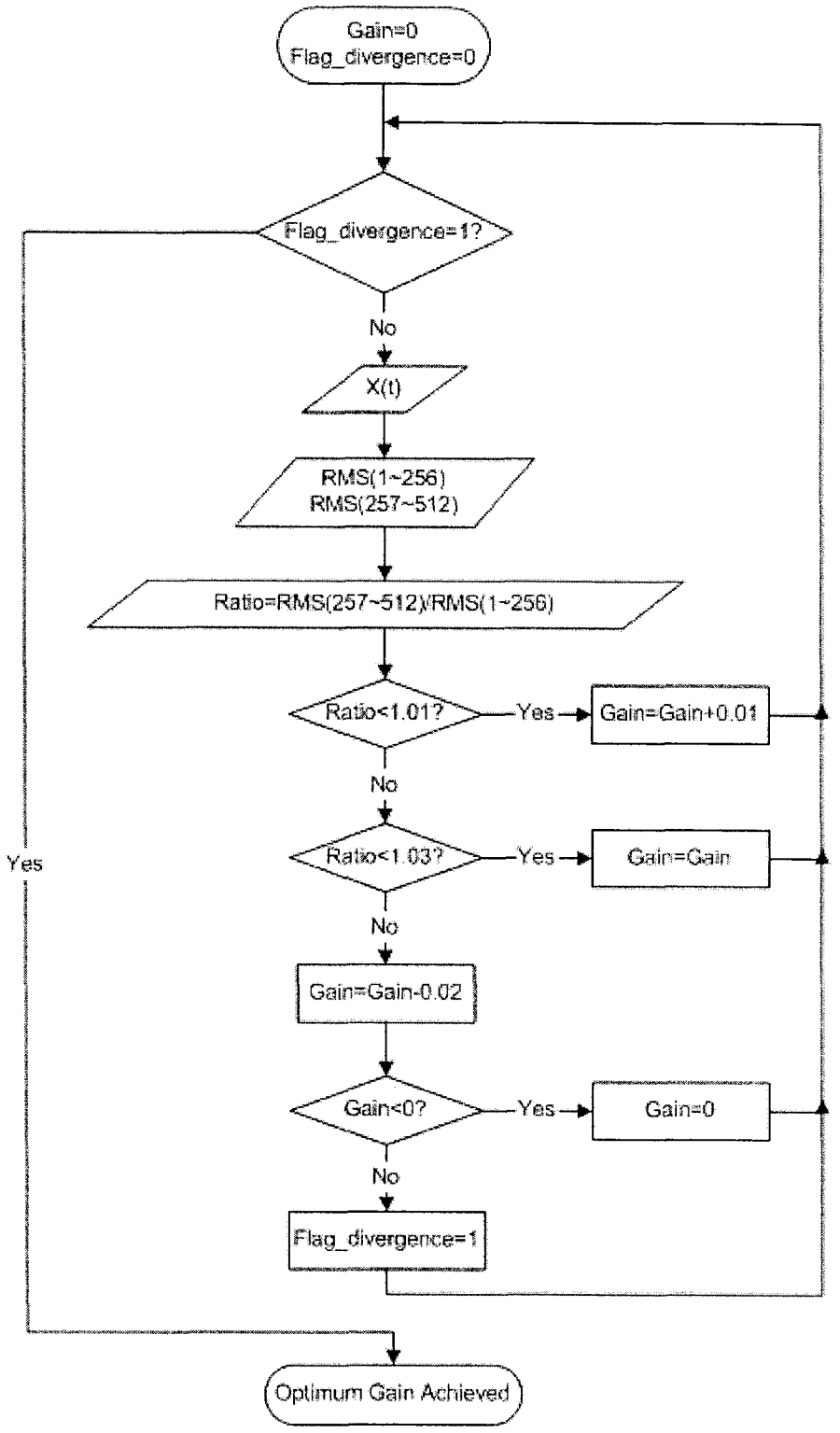

Figure 5.3: Flow chart of the optimum gain tracking program.

The whole simulink model of the computer control, shown in Fig. 5.4, can be described as follows: the sampled acceleration data $\ddot{x}(t)$ of the primary structure are first stored in an S-function named "buffer" until a specified data length (512) is reached. Then the data are passed to an S-function named "optimum gain tracking" where a C program is executed and finally the optimum feedback gain is determined. Meanwhile, the time delay may be obtained as per Eq. (5.6), and then applied to the acceleration signal $\ddot{x}_a(t)$ of the absorber mass. The proportionally amplified time-delayed acceleration signal is used to drive the electromagnets through a current regulator board. As a result, a corresponding control force is generated between the primary system and the absorber system.

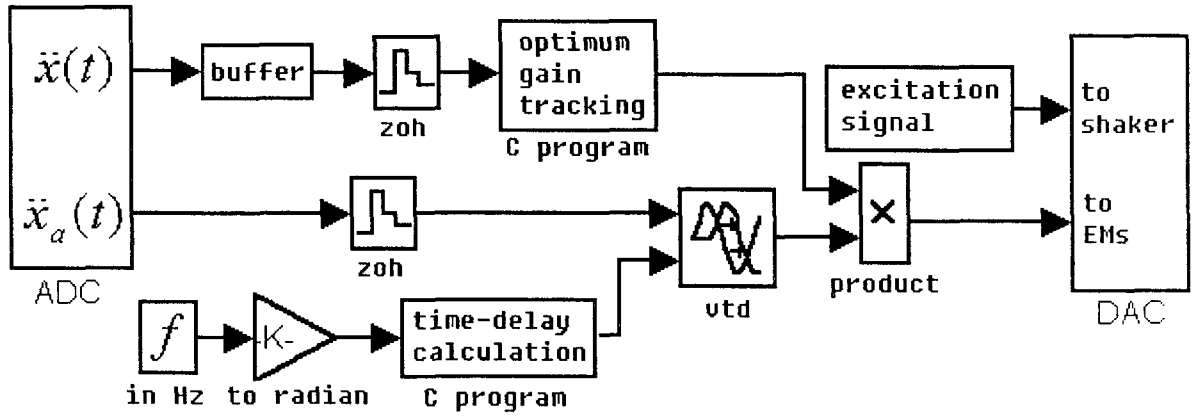

Figure 5.4: Simulink model of the computer control.

5.4 Experimental Results

The experiment was conducted with the exciting frequency was set to 13.3 Hz, 17.1 Hz, respectively, namely the two resonance frequencies obtained experimentally. Figs. 5.5-5.8 show the response of the primary structure without control and with control, in which two scenarios were considered: one, the online optimum-gain tracking strategy was implemented; the other, the actuator with the designed time-delayed control algorithm was activated abruptly at 30 s. It shows that the designed time-delayed vibration absorber can suppress the vibration up to 95% off in terms of the magnitude of the acceleration signal. The alternating voltage applied on the electromagnet windings is demonstrated in the figures as well. It can be seen that the sudden implementation of the control needs a higher peak voltage, a larger quantity of energy input at the moment of the activation; by contrast, the online tuning strategy may gradually suppress the vibration of the primary system and, the energy input is smooth and in a smaller scale.

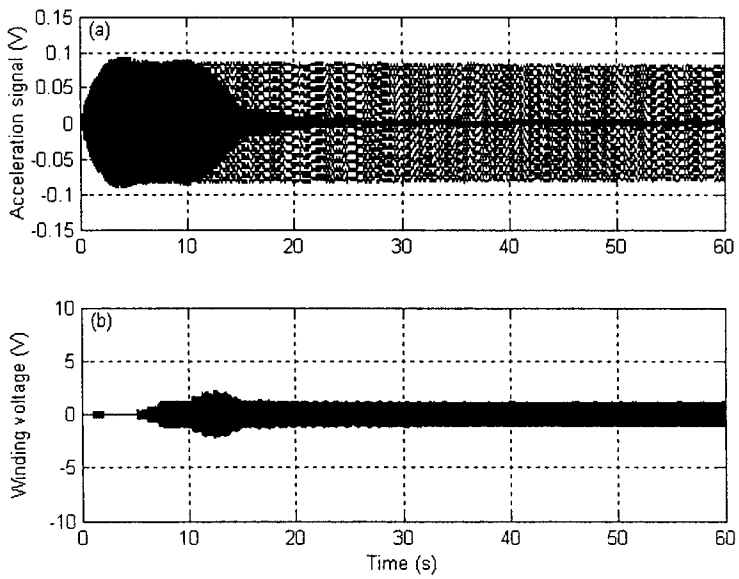

Figure 5.5: Experimental results when the excitation frequency is 13.3 Hz and the online tuning strategy is implemented: (a) the response of the primary system without control (gray line) or with control (dark line); (b) the controlled voltage applied to the electromagnet winding.

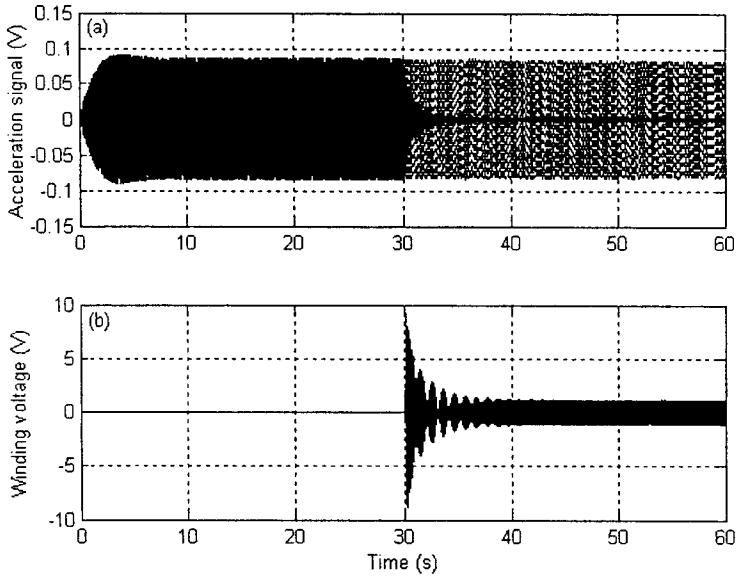

Figure 5.6: Experimental results when the excitation frequency is 13.3 Hz and the designed actuator is activated suddenly at 30 s: (a) the response of the primary system without control (gray line) or with control (dark line); (b) the controlled voltage applied to the electromagnet winding.

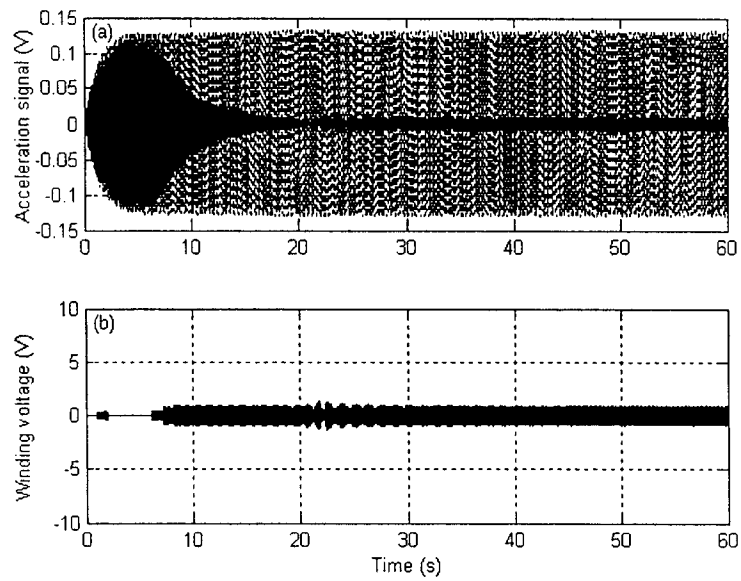

Figure 5.7: Experimental results when the excitation frequency is 17.1 Hz and the online tuning strategy is implemented: (a) the response of the primary system without control (gray line) or with control (dark line); (b) the controlled voltage applied to the electromagnet winding.

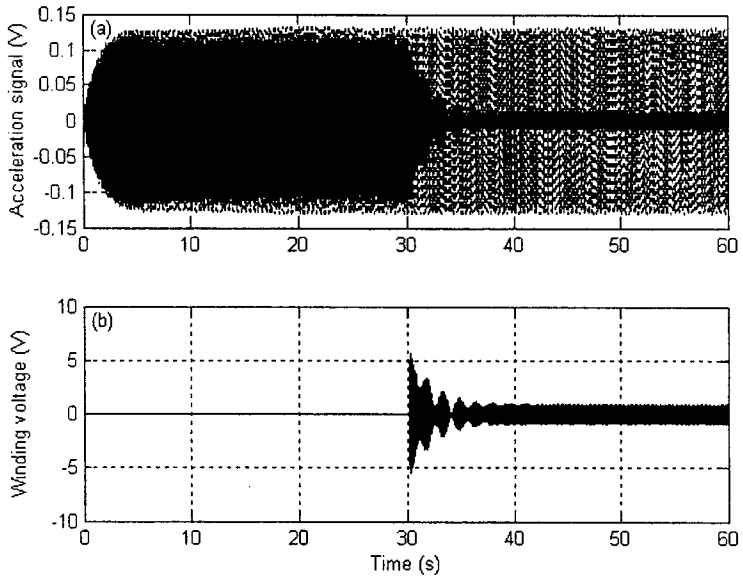

Figure 5.8: Experimental results when the excitation frequency is 17.1 Hz and the designed actuator is activated suddenly at 30 s: (a) the response of the primary system without control (gray line) or with control (dark line); (b) the controlled voltage applied to the electromagnet winding.

As mentioned in the previous section, the upper threshold 1.03 in the optimum gain tracking program was found experimentally by trial-and-error. A too small or too big value of this threshold will make the program defective. If this threshold is too small, it will not compromise the fluctuation of the magnitude of $\ddot{x}(t)$ in the transient response; while, if this threshold is too big, the auto-tuning gain will continuously increase regardless of the fact that the system has been divergently unstable. The experimental results with different settings of this threshold were demonstrated in Fig. 5.9.

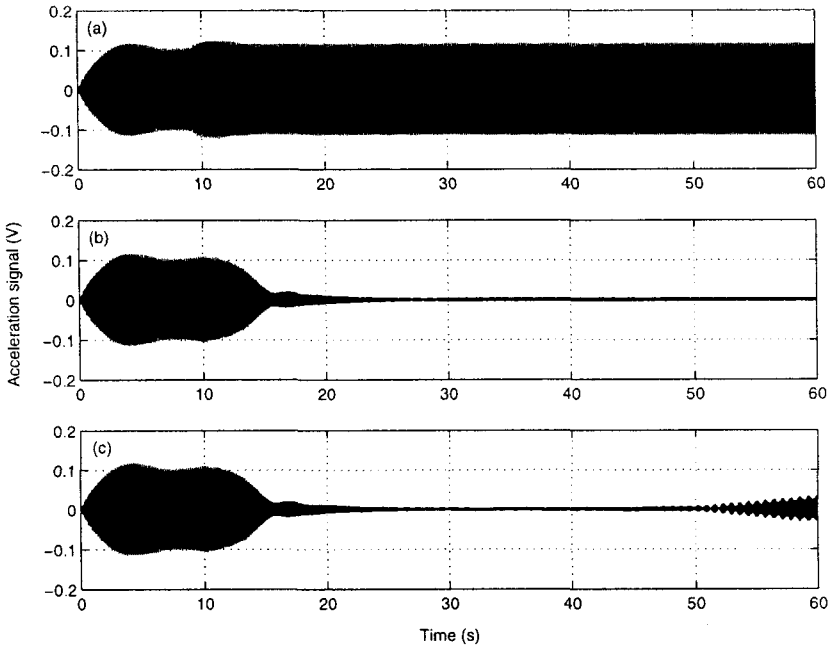

Figure 5.9: The response of the primary mass with different settings of the upper thresholds in auto-tuning program, $w = 13.3$ Hz: (a) threshold 1.014 (b) threshold 1.03 (c) threshold 1.16.

The minimum global crossing gain g_c can be found experimentally. For every exciting frequency, the gain can be increased until the response of the primary mass starts to increase and the system starts running into instability. The experimental results were plotted in Fig. 5.10. This experimental gain is proportional to the calculated gain g_c plotted in Fig. 4.3 except a small portion where the exciting frequency is low.

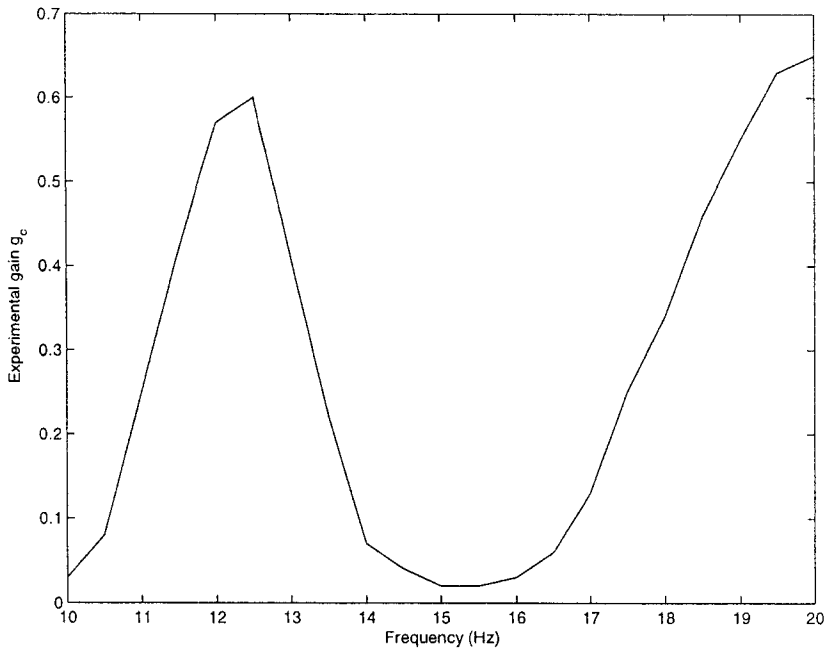

Figure 5.10: The minimum crossing gain g_c obtained experimentally

5.5 Effect of t_s on the Response and the Stability of the Primary System

Provided the optimum actuator feedback gain is fixed, the increase or decrease of the preset time-delay t_s can lead to two situations: the vibration of the primary system may increase and/or the system may go to instability. In order to experimentally demonstrate these effects rendered by the variation of t_s, two scenarios were created. Figure 5.11 shows that the acceleration magnitude of the primary mass was correspondingly increased, as t_s experienced the multi-step changes from 0.021 s to 0.030 s with a step change of 0.003 s. By contrast, when t_s took a step change from 0.021 s to 0.018 s, the system ran into instability and the acceleration magnitude of the primary mass augmented dramatically, as shown in Fig. 5.12. The experimental results are understandable when re-examining Fig. 4.7. The exciting frequency is 13.3 Hz. With the feedback gain unchanged, increasing the time delay t_s will lead to a larger global crossing gain g_c, so the system is still stable, but under the control of the controller with non-optimum parameters; however, decreasing the time delay t_s will lead to a smaller g_c, and the actuator is now working with a feedback gain bigger than this global crossing gain g_c, so the whole system goes to instability.

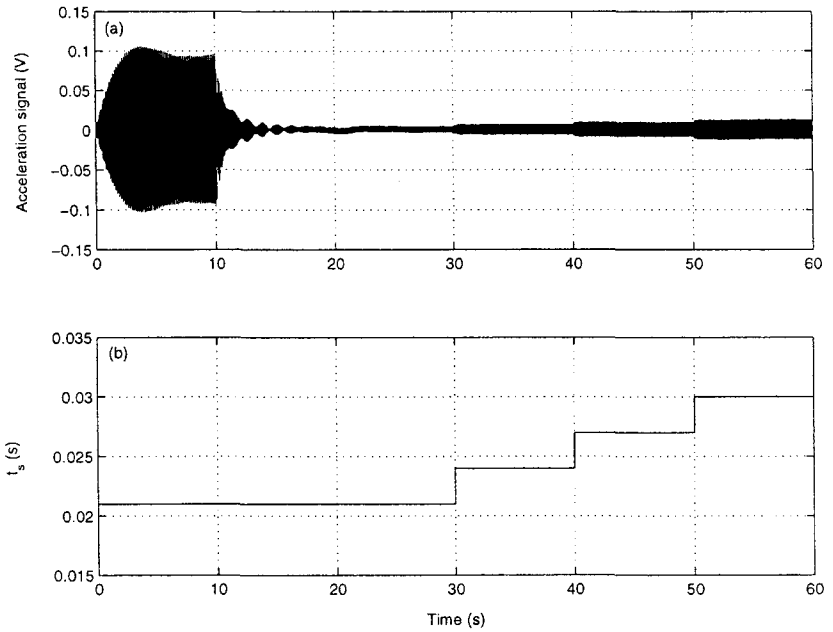

Figure 5.11: Experimental results when t_s experiences the multi-step changes, w = 13.3 Hz: (a) the response of the primary system; (b) the variation of t_s.

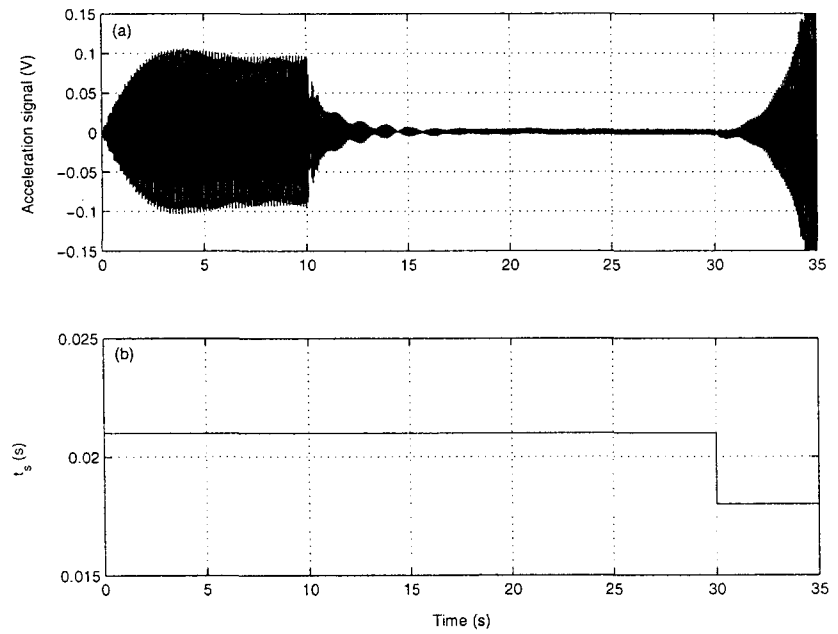

Figure 5.12: Experimental results when t_s experiences a step change, w= 13.3 Hz: (a) the response of the primary system; (b) the variation of t_s.

Chapter 6

Conclusions and Future Work

6.1 Conclusions

Firstly, an electromagnetic vibration absorber (EMVA) has been developed. By varying the current to the electromagnet, the absorber stiffness can be on-line adjusted; as a result, it can cope with a harmonic excitation with a variable frequency. A procedure for the stiffness characterization has been presented. The fundamental theory of electromagnetism has been employed to establish the analytical relation for the variable magnetic stiffness. The analytical relation has been validated experimentally. The effectiveness of the electromagnetic vibration absorber has been tested. The experiment has shown that EMVA is capable of adjusting its frequency such that the tuning condition is satisfied in the event of variation of the exciting frequency. The main advantages of the proposed device lie in its rapid reaction and motionless adjustment. The analysis approaches employed in this study are useful for further optimization of the device and design of any new devices involved in application of electromagnetism. Further, based on the theoretical study in Chapter 3, the following conclusions can be drawn: 1). In computing the flux density, an electromagnet with a thin layer of coils may be modeled as a current carrying cylindrical sheet. When the difference between the outer radius and the inner radius of the coils increases, the approximation error will increase. 2). A permanent magnet with a round cross section harnesses the flux from the electromagnet most efficiently and offers the greatest magnetic stiffness, as a result, the adjustable margin for k_v is enlarged. 3). A permanent magnet with a round cross section results in the greatest negative constant magnetic stiffness due to the interaction between the permanent magnet and the core of the electromagnet. This effect

seems to counteract the effect stated above. However, this counteraction can be compensated by manipulating the constant stiffness created by the absorber beam. 4). In general, the narrower the gap of the electromagnet, the greater and more linear the variable magnetic stiffness.

Secondly, based on a traditional PD control algorithm, a time-delayed vibration control system has been developed to suppress the vibration of the primary system caused by the harmonic excitation. This control system features that the signal feedback may be the response of the absorber system in any form: displacement, velocity and acceleration. The stability issue of the entire system has been discussed. An electromagnetic actuator has been designed and utilized in the experiment to provide a controllable force. An online tuning strategy has been proposed to automatically determine the optimum feedback gain of the control system for the current setup. Both the simulation and the experimental results have shown that the time-delayed control system can significantly reduce the vibration of the primary system. Further, it was found that the average power consumption of this time-delayed vibration absorber was only around 0.2 W.

6.2 Future Work

The tunable electromagnetic vibration absorber proposed in this thesis belongs to a lab work and, its effectiveness in vibration suppression has been demonstrated. The maximum power requirement of this EMVA in the experiment is 20 W. How to make this EMVA applicable in industries becomes the main focus of a future research. Some tentative directions in this regard are the miniaturization of the EMVA, its lower power consumption, the fatigue of the materials, its resistance to the corrosion, the noises and the external impact.

As to the time-delayed vibration absorber, the current experiment setup needs improvements. The damping c of the primary system is not a constant value. When the displacement x is small, c assumes a small value. When the displacement x increases, c takes a large value. This fact may prevent showing the effectiveness of the time-delayed vibration absorber in vibration suppression in the case that the damping c is high. In order to provide a higher and more constant damping c for the primary system, new materials for the plates that form the primary spring need to be found. Further, the practical application of this time-delayed vibration absorber should be investigated as well.

Bibliography

[1] M. A. Franchek, M. W. Ryan and R. J. Bernhard, Adaptive passive vibration control, *Journal of Sound and Vibration*, 189 (1995), 565-585.

[2] C. Buhr, M. A. Franchek, and R. J. Bernhard, Non-collocated adaptive-passive vibration control, *Journal of Sound and Vibration*, 206 (1997), 371-398.

[3] K. Nagaya, A. Kurusu, S. Ikai, and Y. Shitani, Vibration control of a structure by using a tunable absorber and an optimal vibration absorber under auto-tuning control, *Journal of Sound and Vibration*, 228 (1999), 773-792.

[4] N. Varadarajan and S. Nagarajaiah, Response control of building with variable stiffness tuned mass damper using empirical mode decomposition and Hilbert transform algorithm, *16th ASCE Engineering Mechanics Conference*, July 2003, Seattle.

[5] K. Liu, L. Liao, and J. Liu, Comparison of two auto-tuning methods for a variable stiffness vibration absorber, *Transactions of Canadian Society for Mechanical Engineering*, 29 (2005), 81-96.

[6] Daniel J. Inman, *Engineering Vibration*, 2nd Edition, ISBN: 013726142X, Prentice-Hall, New Jersey, 2001.

[7] K. Liu and J. Liu, The damped dynamic vibration absorbers: revisited and new result, *Journal of Sound and Vibration*, 284 (2005), 1181-1189.

[8] W. N. Patten, R. L. Sack, and Q. He, Controlled semiactive hydraulic vibration absorber for bridges, *Journal of Structural Engineering*, 122 (1996), 87-192.

[9] M. D. Symans and M. C. Constantinou, Seismic testing of a building structure with a semi-active fluid damper control system, *Earthquake Engineering and Structural Dynamics*, 26 (1997), 759-777.

[10] P. Dupont, P. Kasturi, and A. Stokes, Semi-active control of friction dampers, *Journal of Sound and Vibration*, 202 (1997), 203-218.

[11] L. Y. Lu, Semi-active modal control seismic structures with variable friction dampers, *Engineering Structures*, 26 (2004), 437-454.

[12] S. B. Choi, H. K. Lee, and E. G. Chang, Field test results of a semi-active ER suspension system associated with skyhook controller, *Mechatronics*, 11 (2001), 345-353.

[13] A. Milecki, Investigation and control of magneto-rehological fluid dampers, *International Journal of Machine Tools & Manufacture*, 41 (2001), 379-391.

[14] B. Erkus, M. Abe, and Y. Fujino, Investigation of semi-active control for seismic protection of elevated highway bridges, *Engineering Structures*, 24 (2002), 281-293.

[15] T. Mizuno and K. Araki, Control system design of a dynamic vibration absorber with an electromagnetic servomechanism, *Mechanical Systems and Signal Processing*, 7 (1993), 293-306.

[16] M. S. Trimboli, R. Wimmel, and E. Breitbach, A quasi-active approach to vibration isolation using magnetic springs, *SPIE*, 2193 (1994), 73-83.

[17] Y. Matsuzaki, T. Ikeda, A. Nae, and T. Sasaki, Electromagnetic forces for a new vibration control system: experimental verification, *Smart Materials and Structures*, 9 (2000),127-131.

[18] C. C. Chen and M. K. Yeh, Parametric instability of a beam under electromagnetic excitation, *Journal of Sound and Vibration*, 240 (2001), 747-764.

[19] S. Yashita and K. Seto, Vibration and noise control using dual dynamic absorbers with magnetic damping, *Proceedings of the third International ISEM Symposium on the Application of Electromagnetic Forces*, Sendai, 1992.

[20] D. Kienholz and S. Pendleton, Demonstration of solar array vibration suppression, *SPIE*, 2193 (1994), 59-72.

[21] K. Liu, J. Liu, and L. Liao, Application of a tunable electromagnetic damper in suppression of structural vibration, Submitted to the *Transaction of the Canadian Society for Mechanical Engineering*, October 2004.

[22] D. J. Craik, *Magnetism: principles and applications*, ISBN: 0471954179, Wiley, New York, 1995.

[23] H. H. Woodson and J. R. Melcher, *Electromechanical Dynamics-Part I: Discrete Systems*, ISBN: 0471959855, John Wiley & Sons, 1968.

[24] M. Kidner and M. J. Brennan, Improving the performance of a vibration neutralizer by actively removing damping, *Journal of Sound and Vibration*, 221 (1999), 587-606.

[25] M. Kidner and M. J. Brennan, Real-time control of both stiffness and damping in an active vibration neutralizer, *Smart Material and Structure*, 10 (2001), 758-769.

[26] Giovanni Caruso, Sergio Galeani and Laura Menini, Active vibration control of an elastic plate using multiple piezoelectric sensors and actuators, *Simulation Modeling Practice and Theory II*, 11 (2003), 403-419.

[27] N. Olgac and B. T. Holm-Hansen, A novel active vibration absorption technique: delayed resonator, *Journal of Sound and Vibration*, 176 (1994), 93-104.

[28] Nejat Olgac and Brian Holm-Hansen, Tunable active vibration absorber: the delayed resonator, *Journal of Dynamic Systems, Measurement, and Control*, 117 (1995), 513-519.

[29] N. Olgac, H. Elmali and S. Vijayan, Introduction to the dual frequency fixed delayed resonator, *Journal of Sound and Vibration*, 189 (1996), 355-367.

[30] Damir Filipovic and Nejat Olgac, Torsional delayed resonator with velocity feedback, *IEEE/ASME Transactions on Mechatronics*, 3 (1998), 67-72.

[31] Mark E. Renzulli, Rajiv Ghosh-Roy and Nejat Olgac, Robust control of the delayed resonator vibration absorber, *IEEE Transactions on Control Systems Technology*, 7 (1999), 683-691.

[32] Hakan Elmali, Mark Renzulli and Nejat Olgac, Experimental comparison of delayed resonator and PD controlled vibration absorbers using electromagnetic actuators, *Transactions of the ASME*, 122 (2000), 514-520.

Appendix A

Further Information on Permanent Magnets

A.1 Definition of Magnetization

The strength of the poles for a PM is found to be proportional to the cross-sectional area or the area of the end faces. Thus the poles appear to be surface poles, with a certain density per unit area. The most apparent way to account for this observation is to postulate the presence of a vector quantity M, directed along the magnet axis, with magnitude M indicative of the magnet strength or magnetization for the particular material, so that the poles appear only to the extent that M intersects the surface. The pole strength is then σ =M·n, with n the outward unit normal to the surface: $\sigma = 0$ along the sides and $\sigma = \pm M$ at the ends ⊥M.

A.2 Fields from Cylindrical PMs

To calculate the fields directly the simplest procedure is to initially carry out a restricted calculation for the field components above one pole face of a cylindrical magnet disposed as in Fig. A.1. The coordinates ρ and θ can then be used for the integration. For the element $\rho d\theta d\rho$ the field is dH_r along r,

$$dH_r = \frac{\sigma}{4\pi} \frac{\rho d\theta d\rho}{r^2} \tag{A.1}$$

where σ is the surface pole density of the PM. Since $r^2 = \rho^2 + z^2$, this leads to

$$dH_r = \frac{\sigma}{4\pi} \frac{\rho d\theta d\rho}{\rho^2 + z^2} \tag{A.2}$$

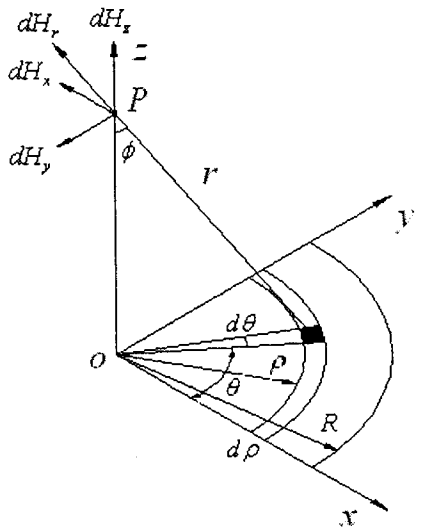

Figure A.1: For the fields from a circle of uniform pole density at a point above one corner.

The contribution of the element to H_z is

$$dH_z = dH_r \cos\phi \tag{A.3}$$

where

$$\cos\phi = \frac{z}{\sqrt{z^2+\rho^2}} \tag{A.4}$$

Mathematical manipulation yields

$$dH_z = \frac{\sigma}{4\pi}\frac{z\rho d\theta d\rho}{(\rho^2+z^2)^{3/2}} \tag{A.5}$$

Integrating w.r.t ρ and θ over the area of the circle to give the contribution from the whole sheet, the component H_z for $\sigma > 0$ is along OZ is

$$H_z = \frac{\sigma}{4\pi}\int_0^{2\pi}\int_0^R \frac{z\rho}{(\rho^2+z^2)^{3/2}} d\rho d\theta = \frac{\sigma}{2}(1 - \frac{z}{\sqrt{R^2+z^2}}) \tag{A.6}$$

Finally, the magnetic field strength at a point P can be found by superposition on the contributions from two pole faces of the PM, which is given as

$$H_z = \frac{\sigma}{2}\left[\frac{z+h}{[R^2+(z+h)^2]^{1/2}} - \frac{z}{[R^2+z^2]^{1/2}}\right] \tag{A.7}$$

It should be noted that, due to the symmetry, the field contributions in other directions are canceled out. Accordingly, the flux density B_z at the same point is represented by

$$B_z = \frac{\mu_0 M}{2}\left[\frac{z+h}{[R^2+(z+h)^2]^{1/2}} - \frac{z}{[R^2+z^2]^{1/2}}\right] \tag{A.8}$$

where h, M are the thickness and magnetization of the PM, respectively. Note that $\sigma = M$.